J. Fluid Mech. (2002), *vol.* 471, *pp.* 169–201.
DOI: 10.1017/S0022112002002185 Printed in the United Kingdom

Theoretical predictions for the elliptical instability in a two-vortex flow

By STÉPHANE LE DIZÈS[1] AND FLORENT LAPORTE[2]

[1]Institut de Recherche sur les Phénomènes Hors Équilibre (IRPHE), 49, rue F. Joliot Curie, BP 146, F-13384 Marseille cedex 13, France

[2]CERFACS, 42, avenue G. Coriolis, F-31057 Toulouse cedex 1, France

(Received 29 October 2001 and in revised form 7 May 2002)

Two parallel Gaussian vortices of circulations Γ_1 and Γ_2, radii a_1 and a_2, separated by a distance b may become unstable by the elliptical instability due the elliptic deformation of their cores. The goal of the paper is to analyse this occurrence theoretically in a general framework. An explicit formula for the temporal growth rate of the elliptical instability in each vortex is obtained as a function of the above global parameters of the system, the Reynolds number Γ_1/ν, and the non-dimensionalized axial wavenumber $k_z b$ of the perturbation. This formula is based on a known asymptotic expression for the local instability growth rate at an elliptical stagnation point which depends on the local characteristics of the elliptical flow and the inclination angle of the local perturbation wavevector at this point. The elliptical flow characteristics are estimated by considering each Gaussian vortex alone in a weak uniform external strain field whose properties are provided by a point vortex modelling of the vortex pair. The inclination angle is obtained from the dispersion relation for the Gaussian vortex normal modes and the local expression near each vortex centre for the two helical modes of azimuthal wavenumber $m = 1$ and $m = -1$ which constitute the elliptical instability global mode. Both the final formula and the hypotheses made for its derivation are tested and validated by direct numerical simulations and large-eddy simulations.

1. Introduction

Two parallel vortices, stable when alone, can become unstable when they are placed close to each other due to the strain field that each vortex induces on the other. This 'elliptical' instability, which is characterized by a three-dimensional deformation of the vortex cores, has been found for both counter-rotating (Leweke & Williamson 1998) and co-rotating vortices (Meunier & Leweke 2001; Meunier 2001). The goal of this paper is to provide an explicit formula for the growth rate of this instability in a general two-vortex flow.

Numerous works on vortex dynamics have focused on the two-dimensional interactions of vortices, particularly those associated with vortex merging. The main objective was to provide physical arguments for the scaling properties of two-dimensional turbulence (see, for instance Couder 1983; Weiss & McWilliams 1993). Two-dimensional interactions are however not limited to vortex merging. Melander, McWilliams & Zabusky (1987) and Trieling, Beckers & van Heijst (1997), among others, demonstrated that other complex phenomena such as straining could also occur when the vortices are not identical. In general, both merging and straining processes occur

when the vortices are sufficiently close. In a three-dimensional flow however, these processes are expected to be modified by the elliptical instability.

Vortices may also be subject to a two-dimensional instability if they are surrounded by a vorticity skirt of opposite sign. This instability often leads to the break up of the vortex in several smaller vortices. This phenomenon is well-documented in geophysical flows where multipolar vortices are often created by this mechanism (see Hopfinger & van Heijst 1993, and references therein). Finally, a single vortex may also be subject to the centrifugal instability if its circulation decreases at some radius. In all these cases, each vortex exhibits complex dynamics which we do not want to consider. For this reason, our analysis focuses on vortices with a Gaussian vorticity profile which are known to be stable with respect to the above instabilities. Other motivations for this choice are provided in the next section.

In fact, the three-dimensional stability of a Gaussian vortex is not fully established. The most recent results are by Prochazka & Pullin (1995) and only concern the two-dimensional stability properties. Even in two dimensions, the evolution of linear perturbations on a Gaussian vortex involves complex shear-diffusion mechanisms as shown by Bernoff & Lingevitch (1994) and Bassom & Gilbert (1998). Recent works by Schecter *et al.* (2000) and Balmforth, Llewellyn Smith & Young (2001) also demonstrated the existence of a damped vortex quasi-mode which directly intervenes in the short-time relaxation process.

In the presence of another vortex, a vortex feels an external strain field which elliptically deforms its core. An asymptotic description of such a vortex in a stationary strain field was first given by Ting & Tung (1965) (see also Moffatt, Kida & Ohkitani 1994). Le Dizès (2000*a*) extended their analysis in order to consider a general rotating strain field which corresponds to the situation for two general interacting vortices. The relevance of this description to two co-rotating vortices is demonstrated in Le Dizès & Verga (2002). Similar results for non-identical vortices will be provided here.

The addition of a third dimension to the vortex interactions modifies the vortex dynamics as the elliptical three-dimensional instability may occur before rapid two-dimensional phenomena such as vortex merging have started (see Meunier & Leweke 2001). The mechanism of the elliptical instability is now well-understood. The instability results from the resonant coupling of two vortex modes with the strain field generated by the other vortex (Moore & Saffman 1975). The instability is called 'elliptical' as it can also be associated with the elliptical nature of the streamlines near the vortex centre (Bayly 1986). The literature is abundant on the subject. A comprehensive list of references is provided in a recent review by Kerswell (2002).

So far, explicit results have been limited to very simple configurations where the flow is uniform. Waleffe (1990) provided the first theoretical prediction for a uniform elliptical flow. Other effects such as stratification, Coriolis forces and magnetic fields were also included in the formula for the maximum growth rate (see Kerswell 2002). The extension to a non-uniform configuration is however non-trivial. The difficulty can be considered to be of the same nature as that in the determination of the global behaviour of a non-parallel flow from its local stability properties (Huerre & Monkewitz 1990). However, experimental and numerical results give us a few important hints (see for instance Leweke & Williamson 1998; Billant, Brancher & Chomaz 1999; Laporte & Corjon 2000). In particular, the maximum growth rate of the elliptical instability seems to be well-predicted by the local stability properties of the vortex near its centre. Eloy & Le Dizès (1999) demonstrated that in a single slightly strained Gaussian vortex, the maximum growth rate of the first instability was within 3% of Waleffe's theoretical prediction for the vortex centre. Here, our

model is based on this assumption, that is the local growth rate in each vortex centre provides the growth rate for the global instability modes. It is validated *a posteriori* by a comparison with direct numerical results and large-eddy simulations.

The paper describes the various steps of the modelling. In § 2, the two-dimensional dynamics of two arbitrary vortices is described. The various parameters governing the dynamics and the stability properties are introduced. Particular attention is paid to the conditions under which the stability of the vortex system can be addressed. The basic assumption is that the vortex system is quasi-steady in a rotating frame and that the axisymmetric part of each vortex profile is approximately Gaussian. Under these assumptions, near its centre each vortex can be considered as a stationary elliptical flow in a rotating frame. The local stability properties of such a flow are reviewed and applied to the vortex system in § 3. The formula for the growth rate is found to depend on two undetermined coefficients, which are the internal strain rate (strain in the vortex centre) and the orientation angle of the local perturbation wavevector. The first coefficient is estimated in § 4 by considering the field generated by the other vortex as a uniform external strain field whose characteristics are obtained by a point-vortex model. The results of Le Dizès (2000*a*), where the relation between external and internal strain rates was obtained, are applied and validated by direct numerical computations. Section 5 is concerned with the determination of the orientation angle of the local perturbation wavevector as a function of the perturbation axial wavenumber. This third step in the model is based on the (Kelvin) normal-mode interpretation of the elliptical instability. We argue that the most unstable elliptical instability modes are necessarily a combination of two Kelvin modes of azimuthal wavenumber $m = 1$ and $m = -1$. This permits us to use the dispersion relation of the vortex in the determination of the last relation. The final result of the model is a simple explicit formula for the growth rate of the instability in each vortex which is illustrated in § 6. This formula is tested in § 7 by a three-dimensional simulation of the vortex system for various flow configurations. Direct numerical simulations are performed for low Reynolds number flows, whereas large-eddy simulations are performed for large Reynolds number flows. The overall agreement between the results of the linear theory and the simulations is found to be satisfactory. The last section concludes the paper and discusses an application of the results in the aeronautical context.

2. Two-dimensional dynamics

In this section, the basic characteristics of the two-dimensional dynamics of two vortices are recalled.

As long as both vortices are localized and far apart, a natural approach is first to assume that each vortex reduces to a single point located at the vortex centre. This procedure provides the large-scale non-viscous dynamics of the system. It requires that viscous effects are negligible at leading order. Under this assumption, one just has to determine the evolution of two point vortices of circulation Γ_1 and Γ_2 which are initially separated by a distance b. It is straightforward to show that b does not vary and that if $\Gamma_1 + \Gamma_2 \neq 0$, the two vortices rotate around each other with an angular frequency

$$\Omega = \frac{\Gamma_1 + \Gamma_2}{2\pi b^2}. \tag{2.1}$$

When $\Gamma_1 + \Gamma_2 = 0$, that is when the vortices have opposite circulations, there is no rotation; the vortices evolve at a constant speed $U = \Gamma_1/(2\pi b)$ along a straight line

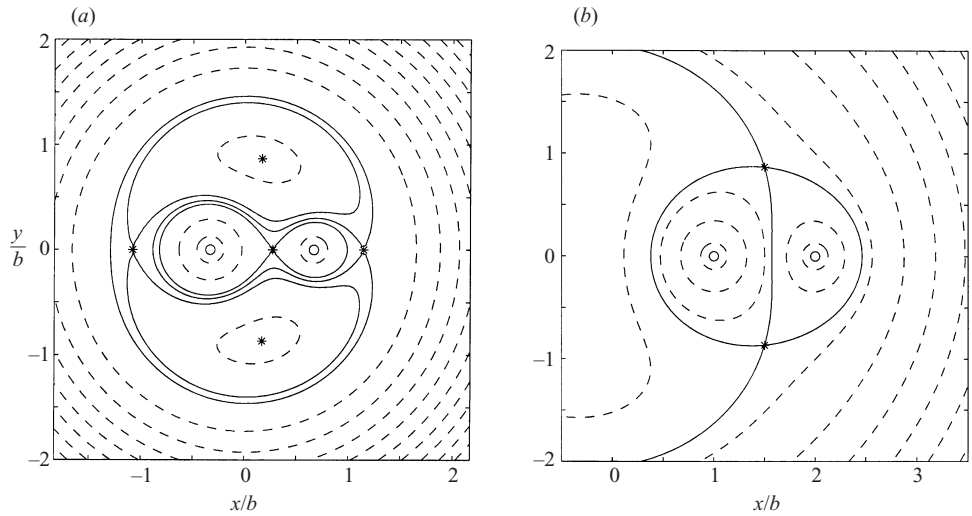

FIGURE 1. Streamline network (in the rotating frame) for (*a*) $\Lambda = 0.5$ and (*b*) $\Lambda = -0.5$. The vortices are indicated by circles and the other stationary points by stars.

perpendicular to the line connecting them. When $\Gamma_1 + \Gamma_2 \neq 0$ the rotation axis of the vortex system is located on the line connecting the two vortices at a distance

$$b_1 = \frac{\Gamma_2 b}{\Gamma_1 + \Gamma_2} \quad \left(\text{resp. } b_2 = \frac{\Gamma_1 b}{\Gamma_1 + \Gamma_2}\right) \tag{2.2}$$

from vortex Γ_1 towards vortex Γ_2 (resp. from vortex Γ_2 towards vortex Γ_1).

In a frame rotating at the angular frequency Ω and centred on the rotation centre, the dynamics is stationary and the streamlines are given by the contour levels of the streamfunction:

$$\Psi = \frac{\Gamma_1}{2\pi}\ln[(x-b_1)^2 + y^2] + \frac{\Gamma_2}{2\pi}\ln[(x+b_2)^2 + y^2] - \frac{\Gamma_1 + \Gamma_2}{2\pi b^2}(x^2 + y^2). \tag{2.3}$$

If one non-dimensionalizes spatial variables with respect to b, it is immediately seen that the streamline network only depends on the relative strength of one vortex with respect to the other, that is on a single parameter

$$\Lambda = \frac{\Gamma_1}{\Gamma_2}. \tag{2.4}$$

Without restriction, one can assume that $|\Gamma_1| \leqslant |\Gamma_2|$ and $\Gamma_1 \geqslant 0$, such that $b_1 \geqslant 0$ and $-1 \leqslant \Lambda \leqslant 1$. The sign of the parameter Λ characterizes the counter- or co-rotating nature of the vortices. The vortices are co-rotating (and with a positive circulation) for positive Λ and counter-rotating for negative Λ. Illustrations of typical streamline networks for co-rotating and counter-rotating vortices are provided in figures 1(*a*) and 1(*b*) respectively.

Note that streamline networks for co-rotating vortices and for counter-rotating vortices are topologically different. Co-rotating vortex streamlines possess three hyperbolic points and two external elliptic stagnation points while counter-rotating vortex streamlines only possess two hyperbolic points and one external elliptic stagnation point. Stagnation points are known to be the seat of local instabilities (Lifschitz & Hameiri 1991). Here, the external elliptic stagnation points are, however, locally stable because there is no absolute vorticity at these points (Le Dizès 2000*b*). On the

other hand, the hyperbolic stagnation points are unstable (Lifschitz & Hameiri 1991; Leblanc 1997). Destabilization of the vortex system by growth of instability near those points could then be possible *a priori*. This possibility is not analysed in the present paper. Instead, we assume that the local growth at the hyperbolic stagnation points does not affect the main characteristics of the elliptical instability. This assumption is checked *a posteriori* by comparing the theoretical predictions with results obtained by numerical simulations.

As long as each vortex is sufficiently localized and confined within the region delimited by the separatrix connected to the closest hyperbolic point, we expect the streamline network to remain qualitatively unchanged whatever the vortex core details. By contrast, the vortex core details, particularly the core size and the vorticity profile, have an important influence on the three-dimensional stability characteristics of the system, as we shall see below. Here, we characterize the vortex core size from the second-order-vorticity moment around the vortex centre by a vorticity radius defined by

$$a_1^2 \equiv \frac{1}{2\Gamma_1}\iint_{D_1}[(x-x_{c_1})^2+(y-y_{c_1})^2]\omega(x,y)\,\mathrm{d}x\,\mathrm{d}y, \tag{2.5}$$

where (x_{c_1}, y_{c_1}) is the vortex centre of vortex Γ_1:

$$x_{c_1} \equiv \frac{1}{\Gamma_1}\iint_{D_1} x\omega(x,y)\,\mathrm{d}x\,\mathrm{d}y, \tag{2.6a}$$

$$y_{c_1} \equiv \frac{1}{\Gamma_1}\iint_{D_1} y\omega(x,y)\,\mathrm{d}x\,\mathrm{d}y. \tag{2.6b}$$

The domain D_1 should contain all the vorticity associated with the vortex Γ_1. This implicitly means that the vortices are not mixed and that there exists a well-defined boundary for each vortex. In practice, we choose for D_1 a disc centred on the vortex centre. Its radius is the distance between the centre and the central hyperbolic point (co-rotating case) or between the centre and the location (between the two vortices) where the vorticity changes sign (counter-rotating case). The circulation Γ_1 should satisfy

$$\Gamma_1 = \iint_{D_1}\omega(x,y)\,\mathrm{d}x\,\mathrm{d}y. \tag{2.7}$$

In a viscous two-dimensional flow, the second-order-vorticity moment of a vortex evolves linearly in time due to viscous diffusion (Batchelor 1967). Each vortex radius therefore satisfies an equation of the form

$$a_1 = \sqrt{a_1^2(0)+4\nu t}. \tag{2.8}$$

Using expression (2.5), two additional length scales a_1 and a_2 are associated with each vortex Γ_1 and Γ_2 which measure the core sizes. The form of the vorticity profiles could provide infinitely many other parameters. In order to limit the number of parameters, here we focus on vortices with a Gaussian vorticity profile only. This choice is motivated by the particular role that Gaussian vortices play in vortex dynamics and turbulence. First, a vortex with a Gaussian profile, the so-called Lamb–Oseen vortex, is known to be the global attractor of any two-dimensional axisymmetric vortex. In other words, all axisymmetric vortices relax by viscous diffusion to the Lamb–Oseen vortex. This property seems to be also satisfied in systems with several vortices. The Gaussian vorticity profile was indeed shown to correspond to the

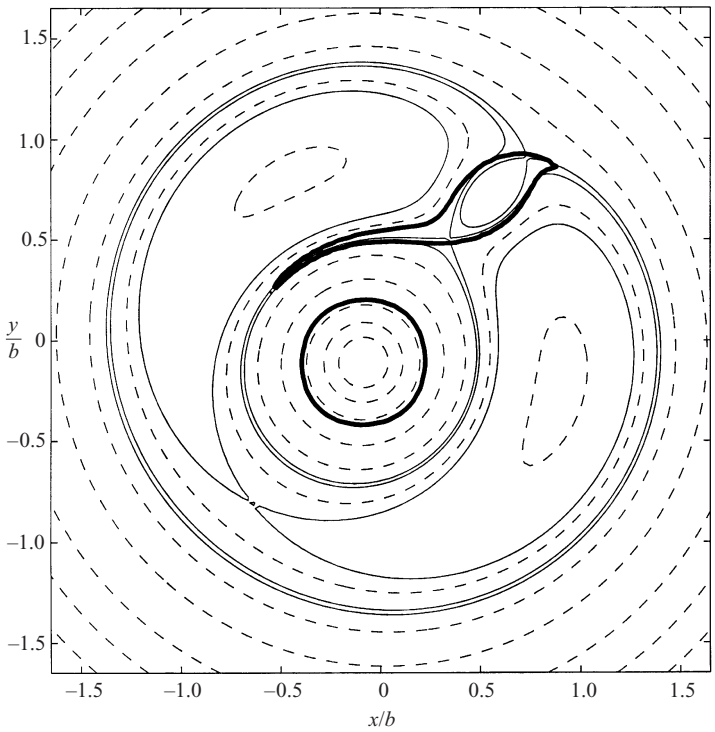

FIGURE 2. Illustration of the straining phenomenon. Streamline network and vortex contour (thick line) of the vortex system in the rotating frame for $\Lambda = 0.2$, $a_1/b = a_2/b = 0.142$, $Re_1 = 2500$. The vorticity level corresponds to 5% of the maximum vorticity for vortex Γ_1.

vortex profiles of the attractive solution obtained for two identical counter-rotating vortices (Sipp, Jacquin & Cossu 2000) and for two identical co-rotating vortices (Le Dizès & Verga 2002). Moreover, Jiménez, Moffatt & Vasco (1996) demonstrated that the Gaussian vortex provides a good description in a statistical sense of vortices encountered in two-dimensional turbulence.

It is also important to point out that the Gaussian profile has the advantage of being unaffected by viscous diffusion. For all times, a Gaussian vortex remains Gaussian. Viscosity only modifies the vortex radius, which evolves according the law given in (2.8). As soon as the Reynolds number is larger than a few hundred, this evolution is sufficiently slow to assume the vortex system to be quasi-stationary in the rotating frame.

The quasi-steadiness of the vortex system is however not guaranteed for all the values of the parameters. For each Λ, there are limitations on the parameters a_1/b and a_2/b. Unfortunately, these limitations are not well-documented except for a few cases. For instance, it is well-known that for two identical vortices ($a_1 = a_2$ and $\Lambda = 1$), rapid time-dependent phenomena leading to vortex merging develop when a/b reaches approximately 0.23 (see Meunier *et al.* 2002). The range of allowed values is therefore $a/b < 0.23$ in that case. The phenomenon of merging also occurs for non-equal vortices as demonstrated by Overman & Zabusky (1982) and Mitchell & Driscoll (1996). In particular, Dritschel & Waugh (1992) and Weiss & McWilliams (1993) obtained merging criteria for vortex patches of same vorticity level but different size. Another phenomenon, called 'straining', has also been observed when one vortex

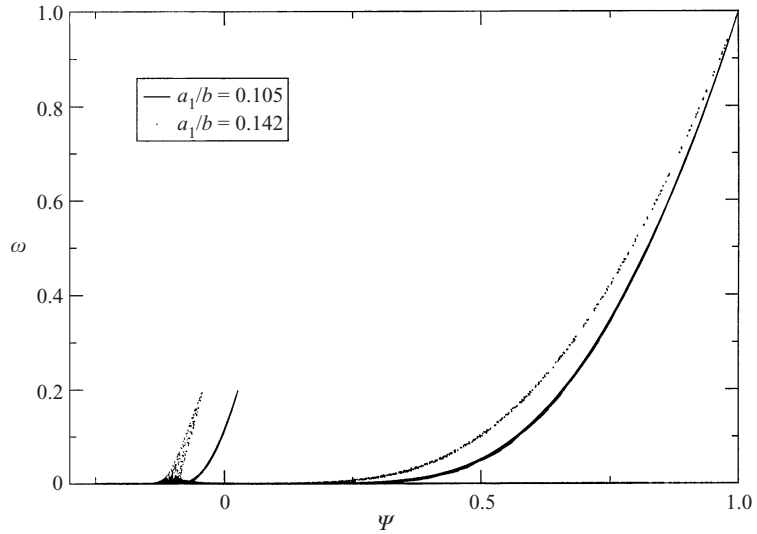

FIGURE 3. Scatter plots (Ψ, ω) of the two-vortex flow in the rotating frame for $\Lambda = 0.2$, $Re_1 = 2500$ and two values of a_1/b: with straining ($a_1/b = a_2/b = 0.142$) and without straining ($a_1/b = a_2/b = 0.1$).

is much larger than the other (i.e. Λ close to zero): the weak vortex is elongated and transformed into a thin vorticity sheet (see for instance Trieling *et al.* 1997; Trieling, Linsen & van Heijst 1998). An illustration of the straining process is provided in figure 2. This picture is obtained by the two-dimensional direct numerical simulation described in § 7. The streamline network is displayed for the vorticity level corresponding to 5% of the maximum vorticity for vortex Γ_1. One clearly sees that while the stronger vortex remains almost axisymmetric (the contour corresponds to 1% of the maximum vorticity for vortex Γ_2), the weaker vortex is strongly distorted and wrapped around the strong vortex. This phenomenon is strongly time-dependent as demonstrated on the scatter plot (streamfunction, vorticity) shown in figure 3. On this figure, two scatter plots for $\Lambda = 0.2$ are superimposed. One corresponds to the configuration displayed on figure 2 ($a_1/b = 0.142$), the second is for a case without straining ($a_1/b = 0.1$). Curves on the right are for the stronger vortex, those on the left are for the weaker vortex. On this plot, the appearance of time-dependent effects is characterized by the thickening of the curve connecting streamfunction to vorticity in the weaker vortex. Note however that a functional relation $\omega = f(\Psi)$ is still present in both vortices before straining or in the stronger vortex during straining. This implies that the flow remains a quasi-stationary solution of the Euler equations in the regions not subject to straining (see also § 7).

Both 'merging' and 'straining' processes limit the range of the parameter values. Unfortunately, there is no clear criterion for the appearance of these phenomena. However, simple conditions can be obtained using the geometry of the streamline network. We have mentioned above that it was important for each vortex to remain well-delimited and separated from the other vortex. This provides constraints on a_1/b and a_2/b. Indeed, vorticity is stripped from the vortex core as soon as it crosses a separatrix connected to a hyperbolic point (see figure 1). This phenomenon, which is all the more important as the Reynolds number becomes large (Le Dizès & Verga 2002), increases vortex leakage across the external hyperbolic points and, in the co-

rotating case, vortex mixing in the central hyperbolic point. In order to minimize these effects, each vortex core should remain within the domain delimited by the closest separatrix connected to a hyperbolic point. This implies conditions on a_1/b and a_2/b which can be written roughly as

$$\text{for } |\Lambda| \geqslant 1/2: \qquad a_1/b < 1/4, \quad a_2/b < 1/4, \tag{2.9a}$$

$$\text{for } |\Lambda| \leqslant 1/2: \qquad a_1/b < \frac{1}{2\sqrt{2}}\sqrt{|\Lambda|}, \quad a_2/b < \frac{1}{2}\left(1-\sqrt{\frac{|\Lambda|}{2}}\right). \tag{2.9b}$$

The above conditions are obtained by requiring that the distance from the vortex centre to the closest hyperbolic point remains at least twice as large as the vortex radius. This choice is arbitrary. It should qualitatively describe how the limitations on a_1/b and a_2/b vary with respect to Λ but it cannot be expected to provide a good quantitative criterion for the threshold of merging or straining. These criteria have been numerically tested for a few configurations. The simulations tend to demonstrate that the real limit is slightly more restrictive than those prescribed by (2.9). Note, in particular, that for the flow parameters of figure 2, straining has started but conditions (2.9*b*) are not invalidated.

For the next sections, it is useful to define a few other quantities relative to each vortex. We shall need the angular velocity in the vortex centre. For the Gaussian vortex Γ_1 it is

$$\mu_1 = \frac{\Gamma_1}{2\pi a_1^2}. \tag{2.10}$$

In the rotating frame, the angular velocity is

$$\tilde{\mu}_1 = \mu_1 - \Omega. \tag{2.11}$$

For each vortex, one can associate a Reynolds number based on the circulation and the kinetic viscosity ν. For vortex Γ_1, it is

$$Re_1 = \frac{\Gamma_1}{\nu}. \tag{2.12}$$

We shall also need the strain rate induced by one vortex on the other. The point-vortex model provides the 'external' strain rate S_{e_1}, which is the strain rate induced by one vortex at the position of the other without taking into account the interaction between strain and vorticity. Expression (2.3) gives

$$S_{e_1} = \frac{\Gamma_2}{2\pi b^2}, \quad S_{e_2} = \frac{\Gamma_1}{2\pi b^2}, \tag{2.13a,b}$$

where S_{e_1} is the strain rate induced by vortex Γ_2 at the position of vortex Γ_1. The 'internal' strain rate which takes into account interactions between strain and vorticity in the vortex core will be estimated in § 4.

3. Elliptical instability in the vortex core

In order to determine the elliptical instability characteristics of the vortex system, it is necessary to focus on each vortex core separately. Using polar coordinates centred on one of the vortex centres, the streamfunction of the quasi-steady vortex system is

(in the rotating frame)

$$\Psi = \Psi_0(r) + \Omega\frac{r^2}{2} + \mathrm{Re}\left\{\sum_{n\geqslant 1}\Psi_n(r)\exp(\mathrm{i}n\theta)\right\}, \tag{3.1}$$

where $\Psi_0(r)$ is a real function associated with the axisymmetric part of the vortex, and $\Psi_n(r)$ complex functions associated with non-axisymmetric deformations of the vortex. The Gaussian vorticity profile assumption means that vortex Γ_1 has an axisymmetric part $\Psi_0(r)$ approximately given by

$$\Psi_0(r) = -\frac{\Gamma_1 a_1}{2\pi}\int_0^r \frac{1-\exp(-(r/a_1)^2)}{r^2}\,\mathrm{d}r. \tag{3.2}$$

It also implicitly assumes that Ψ_0 provides a leading-order approximation of the vortex core.

The choice of the frame moving with the vortex guarantees that the vortex centre is a stagnation point such that Ψ expands near the vortex centre as

$$\Psi \underset{r\to 0}{\sim} -\tilde{\mu}_1\frac{r^2}{2} - S_{\mathrm{i}_1}\frac{r^2}{2}\cos(2\theta+\phi_2) + O(r^3), \tag{3.3}$$

where $\tilde{\mu}_1$ is the angular velocity given by (2.11) and S_{i_1} the internal strain rate. In other words, near its centre, vortex Γ_1 is at leading order an elliptic flow with a streamline eccentricity

$$\varepsilon_1 = \frac{S_{\mathrm{i}_1}}{\tilde{\mu}_1}. \tag{3.4}$$

This observation constitutes the central point of our modelling of the elliptical instability characteristics. The stability characteristics of the flow described by (3.3) are known. In a fixed frame, they have been computed by Bayly (1986) for all ε_1 between 0 and 1. Waleffe (1990) developed an asymptotic theory for small eccentricity and obtained an exact estimate for the growth rate and an interesting expression for the most unstable perturbation. Le Dizès (2000*b*) extended Waleffe's analysis to account for Coriolis effects. The present theory is based on these results which are now briefly reviewed.

In Le Dizès (2000*b*), as well as in Waleffe (1990), the uniform basic flow (3.3) is assumed unbounded, which means that no restrictions associated with boundary conditions or finite size are applied to the perturbations. For small eccentricity ε_1, the basic flow is almost a solid-body rotation. It admits, at leading order in ε_1, velocity–pressure perturbations $(\boldsymbol{u}, p)$ in the form of 'inertial waves':

$$(\boldsymbol{u}, p) = (\boldsymbol{u}_0, p_0)\,\mathrm{e}^{\mathrm{i}\boldsymbol{k}(t)\cdot\boldsymbol{x}}\,\mathrm{e}^{-\mathrm{i}\omega t}, \tag{3.5}$$

where

$$\boldsymbol{k}(t) = k_0\begin{vmatrix}\sin\xi\cos(\tilde{\mu}_1 t+\chi_0)\\ \sin\xi\sin(\tilde{\mu}_1 t+\chi_0)\\ \cos\xi\end{vmatrix} \tag{3.6}$$

and

$$\omega^2 = 4(\tilde{\mu}_1+\Omega)^2\cos^2\xi = 4\mu_1^2\cos^2\xi. \tag{3.7}$$

The wavevector $\boldsymbol{k}(t)$ of these plane waves is of constant norm k_0. It rotates with respect to the vortex axis at the angular frequency $\tilde{\mu}_1$ with a constant inclination

angle ξ. The frequency ω, given by (3.7), is connected to both the inclination angle ξ and the absolute vorticity $2(\tilde{\mu}_1 + \Omega) = 2\mu_1$ of the basic elliptical flow.

Le Dizès (2000*b*) showed that these inertial waves can self-resonate with the strain field when the inclination angle ξ is close to a critical angle ξ_c given by

$$\cos\xi_c = \frac{\tilde{\mu}_1}{2(\tilde{\mu}_1 + \Omega)} = \frac{\mu_1 - \Omega}{2\mu_1}. \tag{3.8}$$

He obtained an expression for the non-viscous growth rate which can be written (at leading order in ε_1) as

$$\sigma_{NV} = \sqrt{\left(\frac{3\tilde{\mu}_1 + 2\Omega}{4(\tilde{\mu}_1 + \Omega)}\right)^4 S_{\mathrm{i}_1}^2 - (\tilde{\mu}_1 - 2(\tilde{\mu}_1 + \Omega)\cos\xi)^2}. \tag{3.9}$$

Viscous effects on the perturbations are easily taken into account by adding the viscous damping rate $\sigma_V = -\nu|\boldsymbol{k}|^2$ (Landman & Saffman 1987). It follows that the maximum growth rate of the inertial wave of axial wavenumber k_z and inclination angle ξ is at leading order

$$\sigma = \sqrt{\left(\frac{3\mu_1 - \Omega}{4\mu_1}\right)^4 S_{\mathrm{i}_1}^2 - (\mu_1 - \Omega - 2\mu_1\cos\xi)^2} - \nu\frac{k_z^2}{\cos^2\xi}, \tag{3.10}$$

where we have replaced $\tilde{\mu}_1$ by $\mu_1 - \Omega$ and $|\boldsymbol{k}|$ by its expression in terms of k_z and $\cos\xi$. Formula (3.10) gives the growth rate of the instability in vortex Γ_1. A similar expression is obtained for the growth rate in vortex Γ_2 by replacing the subscript 1 by 2. In the following, the two formulae for vortices Γ_1 and Γ_2 will provide the stability characteristics of the two-vortex flow with respect to the elliptical instability. In order to simplify the notation, we shall often suppress the subscripts 1 or 2 from the various expressions when there is no ambiguity, e.g. when the results for vortex Γ_1 are obtained by adding the subscript 1 everywhere.

Formula (3.10) has been obtained by expanding the basic flow near a vortex centre and for this reason it only depends on the vortex-centre characteristics. However, some characteristics such as the internal strain rate S_{i} and the orientation angle ξ are so far unknown. The next two sections will be devoted to the determination of these two quantities as a function of the global parameters of the two-vortex system. In particular, we shall see how the vorticity profile and global parameters such as Ω/μ_1 and a_1/b are involved in the definition of these quantities.

In § 4, an approximate expression for S_{i} is obtained using results from Le Dizès (2000*a*). In § 5 a relation is derived between $\cos\xi$ and k_z using an alternative description of the elliptical instability which permits us to take into account the global structure of each vortex.

4. Internal strain rate

The strain rate at the vortex centre or internal strain rate S_{i} should not be confused with the external strain rate S_{e} estimated in § 2. The external strain rate is the strain rate at the vortex centre position assuming that the vortex is not there. It does not take into account the strain–vorticity interactions that are present in the vortex core, while the internal strain rate does.

For instance, in a Rankine vortex (uniform vorticity in a circular patch), it is easy to show that, for small strain rates and in fixed frame, $S_{\mathrm{i}} = 2S_{\mathrm{e}}$ (see Moore & Saffman

1971). In the same conditions, Moffatt *et al.* (1994) showed that $S_i \approx 2.52 S_e$ for a Gaussian vortex. Eloy & Le Dizès (1999) demonstrated that an even larger ratio S_i/S_e can be obtained by altering the vorticity profile. The effect of Coriolis forces on this ratio has been studied only recently in Le Dizès (2000*a*). The expression for S_i we shall use is based on his analysis.

Le Dizès (2000*a*) analysed the deformation of a Gaussian vortex in a weak imposed rotating external strain field. He considered not only the elliptical deformation but also all the higher-order azimuthal corrections generated by a multipolar strain field. As only the elliptic correction is relevant for the elliptical instability, only results concerning the elliptic correction are now described. The elliptic correction corresponds to the term $\Psi_2(r)\exp(2i\theta)$ in expression (3.1) for the basic flow streamfunction centred on one vortex. In Le Dizès (2000*a*), this correction is generated at infinity by a uniform strain field of strain rate S_e, which means that

$$\mathrm{Re}\{\Psi_2(r)\exp(2i\theta)\} \underset{r\to\infty}{\sim} S_e \frac{r^2}{2}\cos(2\theta + \phi_2^\infty).$$

It is also assumed that the external strain rate S_e is small compared to the vorticity in the vortex centre such that the elliptic correction amplitude Ψ_2 is, at leading order, the solution of the linear equation

$$(\Omega_0(r) - \Omega)\left(\frac{\mathrm{d}^2}{\mathrm{d}r^2} + \frac{1}{r}\frac{\mathrm{d}}{\mathrm{d}r} - \frac{4}{r^2}\right)\Psi_2 = \frac{\omega_0'(r)}{r}\Psi_2, \tag{4.1}$$

where Ω_0 and ω_0' are the angular velocity and the vorticity derivative associated with the Gaussian vortex of streamfunction $\Psi_0(r)$ given in (3.2). Internal and external strain rates can be defined from Ψ_2 by

$$S_e = \lim_{r\to\infty}\frac{|\Psi_2(r)|}{r^2}, \quad S_i = \lim_{r\to 0}\frac{|\Psi_2(r)|}{r^2}. \tag{4.2a,b}$$

In the following, it will also be convenient to use the strain ratio

$$K = S_i/S_e. \tag{4.3}$$

In view of (4.2a,b), the dependence of K on the vortex profile is apparent from equation (4.1). This dependence is non-trivial as it results from the complete integration of equation (4.1) from 0 to $+\infty$. There is no general result for an arbitrary vortex profile. Each profile should therefore be analysed on a case-by-case basis. As a consequence, the choice of a particular vorticity profile (here, the Gaussian profile) is a necessary step in order to obtain a quantitative estimate for the strain ratio K.

Equation (4.1) is linear but it may exhibit a singularity if there exists a critical radius r_c where $\Omega_0(r_c) = \Omega$, that is if the angular frequency Ω is in the range of the angular velocity of the vortex. As demonstrated by Le Dizès (2000*a*), the existence of such a singularity has an important influence on the factor K. When there is no singularity, equation (4.1) can be integrated from 0 to $+\infty$, which guarantees that K only depends on the coefficients of the equation. For such a case (the vortex profile being fixed), one thus has $K = K(\Omega/(2\mu))$. By contrast, when equation (4.1) possesses a singularity, this singularity must be resolved in a critical layer by introducing viscous or nonlinear effects. The parameter which characterizes the nature of the critical layer is the so-called Haberman parameter

$$h \equiv \frac{h_c}{\varepsilon^{3/2}Re}, \tag{4.4}$$

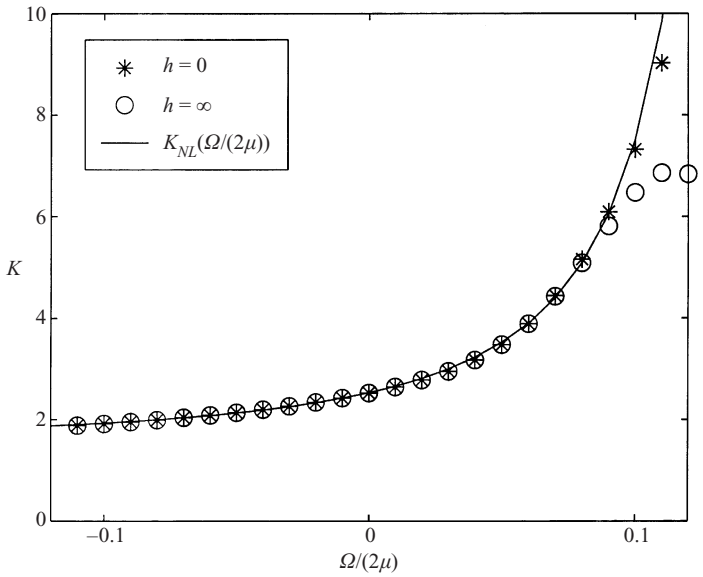

FIGURE 4. Factor $K = S_i/S_e$ versus $\Omega/(2\mu)$. Critical layer singularity exists for $\Omega/(2\mu) > 0$: $h = 0$ and $h = \infty$ correspond to nonlinear and viscous critical layers respectively. A fit (solid line) of the nonlinear critical layer data is provided by expression (4.5).

where ε is the eccentricity streamline defined in (3.4) and h_c a numerical constant close to unity. When h is large, the critical layer is viscous, and the singularity is smoothed by viscous effects. When h is small, the critical layer is nonlinear, and the singularity is smoothed by nonlinear effects. The nature of the critical layer characterizes the jump conditions across the singularity and thus the function $\Psi_2(r)$ in the vortex core. As a consequence, the factor K becomes dependent on the additional parameter h, that is $K = K(\Omega/(2\mu), h)$. Figure 4 displays the behaviour of K as a function of $\Omega/(2\mu)$ for the two extreme cases $h = 0$ and $h = \infty$. The curves for intermediate h are in between. Only values of $\Omega/(2\mu)$ relevant to the two-vortex system are considered.

Interestingly, the nature of the critical layer has an influence on the factor K only for $\Omega/(2\mu) > 0.08$. As shown in Le Dizès (2000*a*), the departure is actually the largest near $\Omega/(2\mu) \approx 0.16$ as $K(\Omega/(2\mu), 0)$ diverges near that value whereas $K(\Omega/(2\mu), \infty)$ remains finite. A good fit of the nonlinear data for $-0.1 < \Omega/(2\mu) < 0.1$ is obtained with the expression (see figure 4)

$$K_{NL}(\Omega/(2\mu)) = 1.5 + 0.038(0.16 - \Omega/(2\mu))^{-9/5}. \tag{4.5}$$

Let us now apply these results to the two-vortex system. *A priori*, the above framework only applies to the limit case where a/b is small such that the external strain field generated by the other vortex is approximately uniform on the vortex core area. In the rest of this section, it is argued that it also provides a good approximation for configurations where a/b is as large as 0.22.

We have seen that the factor K mostly depends on the relative angular velocity $\Omega/(2\mu)$. For vortices Γ_1 and Γ_2, this quantity is given respectively by

$$\Omega/(2\mu_1) = \frac{\Gamma_1 + \Gamma_2}{2\Gamma_1}\left(\frac{a_1}{b}\right)^2 = \frac{1}{2}\left(1 + \frac{1}{\Lambda}\right)\left(\frac{a_1}{b}\right)^2, \tag{4.6a}$$

$$\Omega/(2\mu_2) = \frac{\Gamma_1 + \Gamma_2}{2\Gamma_2}\left(\frac{a_2}{b}\right)^2 = \tfrac{1}{2}(1 + \Lambda)\left(\frac{a_2}{b}\right)^2. \tag{4.6b}$$

For co-rotating vortices ($\Lambda > 0$) both $\Omega/(2\mu_1)$ and $\Omega/(2\mu_2)$ are positive whereas for counter-rotating vortices ($\Lambda < 0$), $\Omega/(2\mu_1)$ is negative and $\Omega/(2\mu_2)$ positive. Under the geometrical constraints (2.9), it is straightforward to show that both $\Omega/(2\mu_1)$ and $\Omega/(2\mu_2)$ remain smaller than 0.083 when $|\Lambda| > 0.1$. For strongly asymmetric configuration, where a_2/b is large and Λ very small, $\Omega/(2\mu_2)$ could *a priori* reach values between 0.08 and 0.12 without violating conditions (2.9). For those cases, the nature of the critical layer could then have an influence on the internal strain rate of the strong vortex Γ_2. However, we expect ε_2 to be larger than $1/Re_2$ in unstable configurations. Thus, the parameter h should be small and the critical layer nonlinear.

For these reasons, we assume in our model that there is a simple linear relation between internal and external strain rates, which is given for each vortex by

$$S_{i_1} = K_{NL}(\Omega/(2\mu_1))S_{e_1}, \quad S_{i_2} = K_{NL}(\Omega/(2\mu_2))S_{e_2}, \tag{4.7a,b}$$

where K_{NL} is defined by (4.5). This model has been tested by Le Dizès & Verga (2002) in the case of two identical co-rotating vortices ($\Lambda = 1$, $a_1 = a_2$). They compared formula (4.7) to the exact internal strain rate obtained by a direct simulation of the interaction of two Gaussian vortices for a/b ranging from 0.05 to 0.23 and different Reynolds numbers between 1000 and 8000. For these values, $\Omega/(2\mu) = (a/b)^2$ varies from 2.5×10^{-3} to 5.3×10^{-2}. Their results demonstrate that (4.7) provides an excellent estimate for $a/b < 0.18$. For $0.18 < a/b < 0.23$, it slightly underestimates the strain rate with a relative error which increases with a/b but remains less than 5%.

Similar results are provided for two non-symmetrical cases in figure 5(a,b). On these plots, the real ratio is obtained by direct simulation. In each case, the simulation is started with $a_1/b = a_2/b = 0.05$ from two axisymmetric Gaussian vortices. The scattering of the numerical values of K for small $|\Omega/(2\mu_1)|$ is associated with the non-viscous adaptation of each vortex with respect to the other. In this initial regime, the internal strain rate exhibits oscillations which are rapidly damped on a non-viscous time scale (Le Dizès & Verga 2002). In the simulations, both the radius and the relative angular frequency of the vortex system evolve in time by viscous diffusion. As already mentioned, this evolution is slow and has no significant influence on the characteristics of the system at a given instant. This evolution is convenient from a numerical point-of-view however as it permits us to cover an important range of parameters by a single simulation (see § 7). Interestingly, one finds numerically that radius and angular frequency are always related to each other by (4.6). This relation is indicated in figure 5 by the thin solid line.

Figure 5 demonstrates that after the initial adaptation process and up to the end of the simulation, which corresponds to the beginning of straining, good agreement between the numerics and the model is obtained.

For other values of Λ, a similarly good agreement has also been observed which makes us confident of the validity of the model.

5. Wavenumber selection

The stability analysis of § 3 has provided an expression for the instability growth rate as a function of the inclination angle ξ of the inertial wavevector in the vortex core. So far, there has been no restriction on ξ. The goal of this section is to show that ξ can take only prescribed values which depend on the axial wavenumber of the perturbation. For this purpose, we shall use an alternative description of the elliptical instability based on the resonant coupling of vortex normal modes ('Kelvin modes') with the strain field. Such a description was first presented for general vortices by

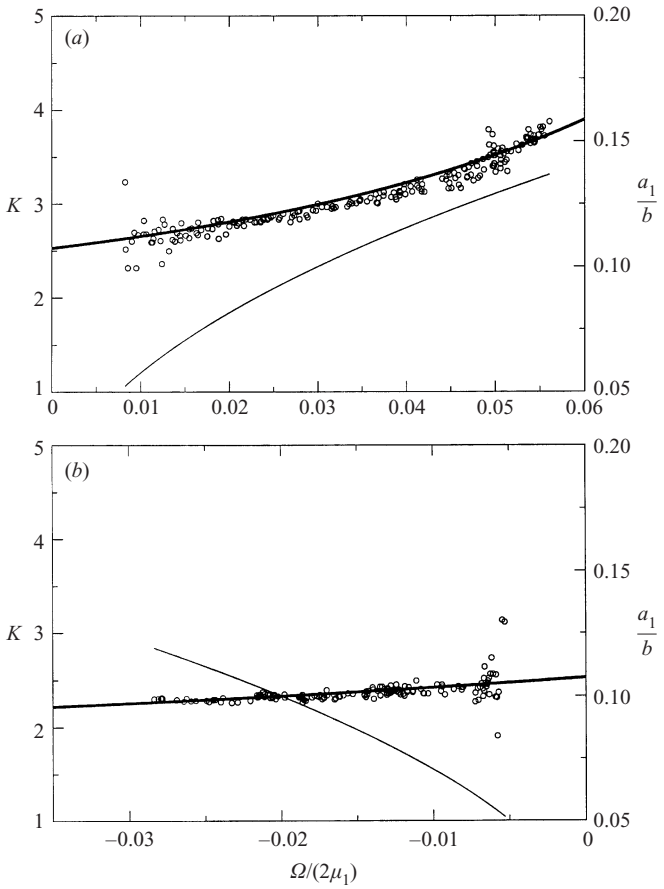

FIGURE 5. Strain ratio K in the centre of vortex Γ_1 for (*a*) $\Lambda = 0.2$ and (*b*) $\Lambda = -0.2$. Symbols ($\circ$) are the ratio of the numerically calculated internal strain rate and $\Gamma_2/(2\pi b^2)$. The thick line is the theoretical prediction $K = K_{NL}(\Omega/2\mu_1)$ defined by (4.5). As explained in the text, the numerical results in each figure are obtained by a single simulation starting from $a_1/b = a_2/b = 0.05$ at $Re_1 = 2500$. The computed relation between the relative angular frequency $\Omega/(2\mu_1)$ and a_1/b is drawn as a thin line using the right-hand vertical axis.

Moore & Saffman (1975). Specific results for a Gaussian vortex can be found in Eloy & Le Dizès (1999) and Sipp (1999). The main ideas of Moore & Saffman's analysis are now presented.

As in § 3, it is assumed that each vortex is only slightly deformed by the field induced by the other vortex. This means that, in (3.1), all the non-axisymmetric terms $\Psi_n(r)$, $n \geqslant 1$ are small compared to the axisymmetric term Ψ_0. Moreover, it is assumed that among these non-axisymmetric terms, $\Psi_2(r)$ is dominant in the vortex core such that only the (elliptical) instability induced by this term is considered. Under these conditions, the vortex is at leading order axisymmetric. Thus, it possesses velocity–pressure perturbations $(\boldsymbol{u}, p)$ in the form of normal (Kelvin) modes:

$$(\boldsymbol{u}, p) = (\boldsymbol{u}_0(r), p_0(r))\, \mathrm{e}^{\mathrm{i}k_z z + \mathrm{i}m\theta - \mathrm{i}\omega t}, \tag{5.1}$$

where (k_z, m, ω) are the axial wavenumber, the azimuthal wavenumber and the frequency of the Kelvin mode.

In Moore & Saffman's analysis, the elliptical instability occurs when two neu-

tral Kelvin modes (k_1, m_1, ω_1) and (k_2, m_2, ω_2) are resonantly coupled by the elliptic correction. Here, the elliptic correction is stationary in the rotating frame. In the fixed frame, unlike Moore & Saffman's case, the elliptic correction is therefore not stationary. Using expression (3.1), it can be written as $\mathrm{Re}\{\Psi_2(r)\exp(2\mathrm{i}(\theta - \Omega t))\}$. The condition of coupling thus yields the following conditions of resonance:

$$k_1 - k_2 = 0, \tag{5.2a}$$

$$m_1 - m_2 = 2, \tag{5.2b}$$

$$\omega_1 - \omega_2 = 2\Omega. \tag{5.2c}$$

When these conditions are satisfied, there is instability and the instability mode is at leading order the sum of the two resonant Kelvin modes. In this description, it is therefore clear that the stability analysis mainly reduces to the study of the resonance condition for the Kelvin modes.

Eloy & Le Dizès (2001) studied these conditions for all azimuthal wavenumbers for a Rankine vortex in the non-rotating case ($\Omega = 0$). They showed that there exist infinitely many resonant configurations for each pair of azimuthal wavenumbers $(m_1, m_1 - 2)$ and they computed the growth rate of the most unstable ones using Moore & Saffman's method. Interestingly, they demonstrated that the most unstable configurations have a frequency close to $\omega_c = (m_1 + m_2)\mu/2 = (m_1 - 1)\mu$ and a growth rate approximately equal to the most unstable growth rate obtained from the inertial wave estimate (3.9). Le Dizès (2000*b*) provided an explanation for this result by connecting the Kelvin modes to the inertial waves seen in § 3. He showed that the Kelvin modes in the vortex core were indeed a sum of most unstable inertial waves if the resonant frequency satisfied the above condition. For the rotating case, he obtained the following condition on the frequencies:

$$\omega_1 \approx \frac{m_1 + m_2}{2}\mu + \Omega = (m_1 - 1)\mu + \Omega, \tag{5.3a}$$

$$\omega_2 \approx \frac{m_1 + m_2}{2}\mu - \Omega = (m_2 + 1)\mu - \Omega. \tag{5.3b}$$

We shall see below that the same condition also applies for a general vortex once one requires the resonant Kelvin modes to be a sum of the most unstable inertial waves near the vortex centre. The more restrictive conditions (5.3*a*, *b*) should therefore be considered in order to be able to connect the resonant Kelvin modes to the unstable inertial waves analysed in § 3. This would also provide a consistent justification of the use of formula (3.10) for the instability growth rate.

Let us now analyse these conditions in our case. Although the Kelvin modes are known for a Rankine vortex, very few results are available for a Gaussian vortex. Recent results by Sipp (1999) demonstrate that unlike the Rankine vortex, the Gaussian vortex exhibits (linear) Kelvin modes which are damped even in the large Reynolds number limit. The damping character is associated with the presence of a viscous critical layer singularity in the perturbation spatial structure. The fine structure of such a singularity is not known but it is of the same nature as for the basic flow correction studied in the previous section: it occurs when the angular frequency is within the range of the angular velocity of the vortex, that is when $0 < \omega/m < \mu$. Sipp (1999) obtained his numerical results by integrating the non-viscous perturbation equation on a contour in the complex plane which avoids the critical point singularity

as is done for shear flow perturbations (see for instance Lin 1955). His results were recently confirmed by Fabre (2002) with a viscous spectral code.

Outside the critical layer range, Gaussian-vortex Kelvin modes seem to share similar properties as Rankine-vortex Kelvin modes (Sipp 1999): their frequencies are real (for large Reynolds numbers) and satisfy $(m-2)\mu \leqslant \omega \leqslant (m+2)\mu$. Moreover, the dispersion relation of Kelvin modes possesses the following important symmetry property: it is invariant under the transformation

$$k \to k, \quad m \to -m, \quad \omega \to -\omega^*. \tag{5.4}$$

If one excludes from the analysis Kelvin mode frequencies in the critical layer range, one immediately sees that

(i) for $0 < \Omega \leqslant \mu$, conditions (5.2a,b) and (5.3a,b) cannot be satisfied by any pair of Kelvin modes;

(ii) for $-\mu < \Omega \leqslant 0$, conditions (5.2$a,b$) and (5.3$a,b$) can only be satisfied by the 'bending' Kelvin modes $m_1 = 1$, $m_2 = -1$.

Strictly speaking, the first assertion implies that there should be no Kelvin mode resonance in co-rotating vortex systems. This would be a very disappointing result in contradiction with known experimental evidence (Meunier 2001; Meunier & Leweke 2001).

The exclusion of the whole critical layer range is therefore excessive. Indeed, one can imagine that conditions (5.2a,b) and (5.3a,b) could be satisfied at leading order in the critical range if the damping rates of the resonant Kelvin modes are small. It turns out that this occurs for the couple $(m_1 = 1, m_2 = -1)$ for small positive Ω/μ. In fact, Sipp's computations demonstrate that the damping rate of the first bending Kelvin modes (i.e. of small wavenumber) is negligible as long as their frequency satisfies $\omega/(2\mu) < 0.06$ (Sipp 1999). This peculiarity may be connected to the fact that, for these frequencies, the critical point singularity is far from the vortex centre and in a region where the way the singularity is smoothed has no influence on the mode characteristics. For two-dimensional modes, Briggs, Daugherty & Levy (1970) showed that in such cases the damping rate was proportional to the vorticity gradient at the critical point (see also Le Dizès 2000a). Such a result for three-dimensional Kelvin modes would be consistent with Sipp's observation.

In the following, only the resonance of the bending modes $m_1 = 1$ and $m_2 = -1$ is considered. This is consistent with the above considerations, experimental evidence (Meunier 2001) and the numerical results presented in the next section. The symmetry property (5.4) of the dispersion relation guarantees that condition (5.3b) is satisfied once (5.3a) is satisfied, so only one of the two conditions need be considered.

On figure 6 the frequency of the first three bending Kelvin modes ($m = 1$) obtained for infinite Reynolds numbers is plotted as a function of the non-dimensionalized wavenumber $k_z a$. For $-0.06 < \omega/(2\mu) < 0.06$, a good estimate for the frequency of the first few branches (at least the first three branches) is obtained with the linear fit

$$\frac{\omega_n}{2\mu} = \frac{(2.26 + 1.69n) - k_z a}{14.8 + 9n}, \tag{5.5}$$

where the integer $n = 0, 1, 2, \ldots$ is the index of the branch. This expression will be used in the general formula for the growth rate. One therefore should keep in mind that it is an estimate of the dispersion relation which only applies for $-0.06 < \omega/(2\mu) < 0.06$, that is for wavelengths of the nth branch satisfying

$$1.37 + 1.15n < k_z^{(n)} a < 3.15 + 2.23n. \tag{5.6}$$

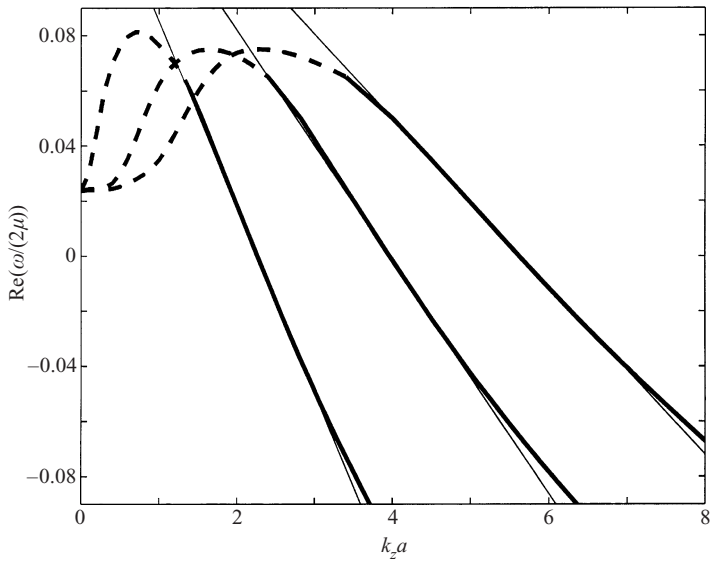

FIGURE 6. Linear dispersion relation for the Kelvin mode $m = 1$ ($Re = \infty$). Thick lines are numerical results for the first three branches $\mathrm{Re}(\omega/2\mu) = f(k_z a)$ as obtained by Sipp (1999). The mode is almost neutral ($\mathrm{Im}(\omega/2\mu) < 0.01$) on the solid part of the curve and strongly damped on the dashed part. Thin solid lines are linear fits given by (5.5) for $n = 0, 1, 2$.

It is important to point out that expression (5.5) is a restriction on the perturbations associated with global effects. In particular, the discretization of the frequencies results from the finite radius of the vortex. Different relations are expected for other vortex profiles but they should be always discrete if the vortex radius is finite.

A relation between the frequency of the Kelvin mode and the inclination angle ξ of the inertial waves described in § 3 can now be obtained by analysing the resonant Kelvin modes near the vortex centre. A simple approximation of the resonant bending modes ($m_1 = 1, m_2 = -1$) is provided by expanding the perturbation equations near the vortex centre. For instance, consider the equation for the pressure of the Kelvin mode (k_z, m, ω) (see Saffman 1992, p. 244): for the pressure amplitude p_0 it becomes near $r = 0$:

$$\frac{\mathrm{d}^2 p_0}{\mathrm{d}r^2} + \frac{1}{r}\frac{\mathrm{d}p_0}{\mathrm{d}r} + \left(k_z^2 \frac{\Delta_m}{\sigma_m^2} - \frac{m^2}{r^2}\right) p_0 = 0, \tag{5.7}$$

where

$$\Delta_m = 4\mu^2 - \sigma_m^2, \tag{5.8a}$$

$$\sigma_m = m\mu - \omega. \tag{5.8b}$$

The bounded solution of (5.7) is

$$p_0 = \mathrm{J}_m(\beta_m r) \tag{5.9}$$

with

$$\beta_m^2 = k_z^2 \frac{\Delta_m}{\sigma_m^2}. \tag{5.10}$$

Using the following expression for the Bessel function $\mathrm{J}_m(z)$:

$$\mathrm{J}_m(z) = \frac{1}{2\pi \mathrm{i}^m} \int_0^{2\pi} \mathrm{e}^{\mathrm{i}z\cos a}\, \mathrm{e}^{\mathrm{i}ma}\, \mathrm{d}a,$$

the expression for both resonant Kelvin modes $m = 1$ and $m = -1$ deduced from (5.9) can be written, in the frame rotating at the angular frequency Ω, as a sum of inertial waves (3.5) provided that (see Waleffe 1990)

$$\beta_m = k_0 \sin\xi, \tag{5.11a}$$

$$k_z = k_0 \cos\xi, \tag{5.11b}$$

$$(\omega - m(\Omega + \tilde{\mu}))^2 = 4(\Omega + \tilde{\mu})^2 \cos^2\xi. \tag{5.11c}$$

Note that these expressions are also compatible with (5.8) and (5.10) since $\mu = \tilde{\mu} + \Omega$. By contrast with expression (5.5), these relations do not depend on the vortex profile as it is only based on a local analysis. They can be considered as simple conditions of compatibility of two representations of the same perturbation near the vortex centre.

If one writes (5.11c) for the mode $m = 1$ as

$$\cos\xi = \frac{\mu - \omega}{2\mu}, \tag{5.12}$$

expression (5.5) for the frequency leads to the relation between $\cos\xi$ and k_z we were seeking:

$$\cos\xi = \frac{1}{2} - \frac{(2.26 + 1.69n) - k_z a}{14.8 + 9n}, \quad n = 0, 1, 2, \ldots . \tag{5.13}$$

6. Theoretical formula for the elliptic instability growth rate

If we collect the results of the previous sections, we obtain a formula for the elliptic instability growth rate in each vortex as a function of the perturbation wavenumber $k_z b$ and the global parameters of the vortex system, that is a_1/b, a_2/b, $\Lambda = \Gamma_1/\Gamma_2$, $Re_1 = \Gamma_1/\nu$ (or $Re_2 = \Gamma_2/\nu$). If the growth rate is normalized by the global turnover time of the vortex system $t_g = 2\pi\Omega = 4\pi^2 b^2/|\Gamma_1 + \Gamma_2|$, we obtain the following formulae for each branch $n = 0, 1, 2, \ldots$:

$$\sigma_1^* = \frac{2\pi}{|1+\Lambda|}\sqrt{\left(\frac{3}{4} - \frac{\Omega_1}{2}\right)^4 K_{NL}^2(\Omega_1) - \frac{4\Lambda^2 b^2}{a_1^2}(\tfrac{1}{2} - \Omega_1 - \cos\xi_1^{(n)})^2} - \frac{4\pi^2|\Lambda|(k_z b)^2}{Re_1|1+\Lambda|\cos^2\xi_1^{(n)}}, \tag{6.1a}$$

$$\sigma_2^* = \frac{2\pi|\Lambda|}{|1+\Lambda|}\sqrt{\left(\frac{3}{4} - \frac{\Omega_2}{2}\right)^4 K_{NL}^2(\Omega_2) - \frac{4b^2}{\Lambda^2 a_2^2}(\tfrac{1}{2} - \Omega_2 - \cos\xi_2^{(n)})^2} - \frac{4\pi^2(k_z b)^2}{Re_2|1+\Lambda|\cos^2\xi_2^{(n)}}, \tag{6.1b}$$

where

$$\cos\xi_{1,2}^{(n)} = \frac{1}{2} - \frac{(2.26 + 1.69n) - k_z a_{1,2}}{14.8 + 9n}, \quad n = 0, 1, 2, \ldots,$$

$$K_{NL}(x) = 1.5 + 0.038\,(0.16 - x)^{-9/5},$$

$$\Omega_1 = \Omega/(2\mu_1) = \frac{(1+\Lambda)a_1^2}{2\Lambda b^2}, \quad \Omega_2 = \Omega/(2\mu_2) = \frac{(1+\Lambda)a_2^2}{2b^2}.$$

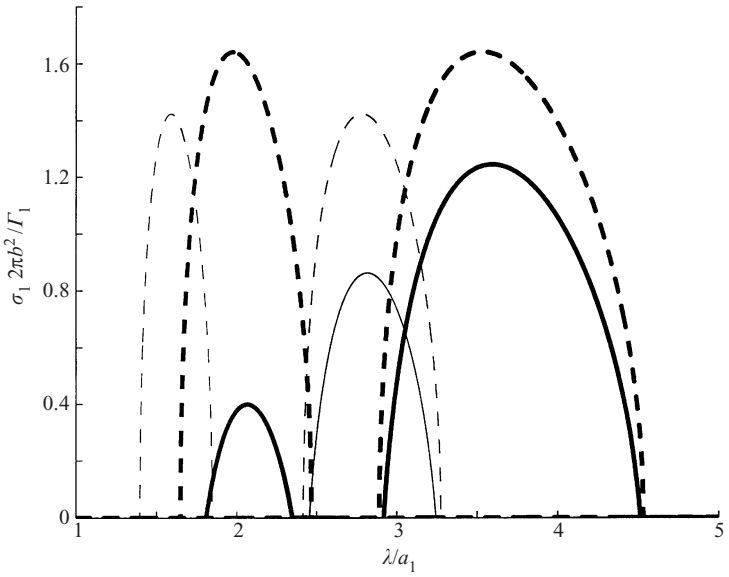

FIGURE 7. Comparison of the stability characteristics of co-rotating vortices and counter-rotating vortices for Reynolds numbers $Re = 7000$ (continuous lines) and $Re = \infty$ (dashed lines). The thick lines are for co-rotating vortices ($\Lambda = 1$) with $a_1/b = a_2/b = 0.18$. The thin lines are for counter-rotating vortices ($\Lambda = -1$) with $a_1/b = a_2/b = 0.18$. Only the first two branches ($n = 0, 1$) are plotted. All the other branches are damped for $Re = 7000$.

Naturally, the normalization by t_g is not adequate for counter-rotating vortices of the same intensity ($\Lambda = -1$). In that case, one can, for instance, use the time associated with the translational motion: $t_c = b/U = 2\pi b^2/|\Gamma_1|$. This leads to the following formulae for $\Lambda = -1$:

$$\sigma_1 t_c = \sqrt{\left(\tfrac{3}{4}\right)^4 K_{NL}^2(0) - \frac{4b^2}{a_1^2}\left(\tfrac{1}{2} - \cos\xi_1^{(n)}\right)^2} - \frac{2\pi(k_z b)^2}{Re_1 \cos^2\xi_1^{(n)}}, \tag{6.2a}$$

$$\sigma_2 t_c = \sqrt{\left(\tfrac{3}{4}\right)^4 K_{NL}^2(0) - \frac{4b^2}{a_2^2}\left(\tfrac{1}{2} - \cos\xi_2^{(n)}\right)^2} - \frac{2\pi(k_z b)^2}{Re_2 \cos^2\xi_2^{(n)}}, \tag{6.2b}$$

where $K_{NL}(0) \approx 2.52$. Before showing specific comparisons with the numerics, it may be useful to illustrate the above formulae by some examples. For instance, it is clear that the elliptic instability is affected by the rotation of the vortex pair. This effect is illustrated on figure 7 where the growth rate (normalized by t_c) is plotted as a function of the perturbation wavenumber for two co-rotating and two counter-rotating vortices of the same a/b and the same Re. As expected from the above discussions, the instability bands are shifted towards larger wavelengths for the co-rotating vortices. This has an effect on the viscous damping which then becomes smaller. The non-viscous growth rate is also increased by the rotation of the pair. These two effects make co-rotating vortices more unstable than counter-rotating vortices. On figure 7, one sees for instance that, for $Re = 7000$ and $a/b = 0.18$, the co-rotating vortices exhibit two instability bands, while the counter-rotating vortices are unstable in a single thin band.

The critical Reynolds number for instability is immediately obtained from (6.1).

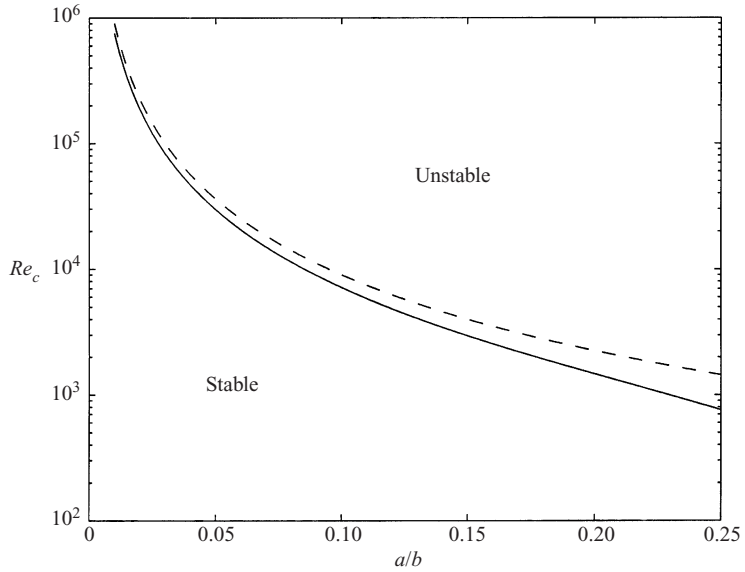

FIGURE 8. Critical Reynolds number versus a/b for two identical co-rotating vortices ($\Lambda = 1$, $a_1 = a_2 = a$; solid line) and two identical counter-rotating vortices ($\Lambda = -1$; $a_1 = a_2 = a$; dashed line).

One obtains for each vortex

$$Re_{1c} = \frac{2\pi|\Lambda|(2.26 - 14.8\Omega_1)^2 b^2}{(1/2 - \Omega_1)^2(3/4 - \Omega_1/2)^2 K_{NL}(\Omega_1) a_1^2}, \tag{6.3a}$$

$$Re_{2c} = \frac{2\pi(2.26 - 14.8\Omega_2)^2 b^2}{(1/2 - \Omega_2)^2(3/4 - \Omega_2/2)^2 K_{NL}(\Omega_2)|\Lambda| a_2^2}. \tag{6.3b}$$

One can see from these formulae that the critical Reynolds number for instability in vortex Γ_1 is roughly proportional to $(b/a_1)^2|\Gamma_1/\Gamma_2|$. This implies that between two vortices of the same radius, the weaker vortex becomes unstable for a smaller value of the Reynolds number. The comparison of the critical Reynolds number for co-rotating vortices and counter-rotating vortices is made on figure 8. Again, as noted above, one can observe that co-rotation enhances the instability: two identical co-rotating vortices become unstable for a smaller Reynolds number than two identical counter-rotating vortices.

7. Comparisons with numerical predictions

In this section, formulae (6.1a, b) are tested using numerical simulations of the instability. Two complementary tests are considered. The first one is performed by large-eddy simulation (LES) methods for very high Reynolds number configurations ($Re > 10^5$) which are relevant to aeronautical applications (see discussion in the next section). The other is performed by direct numerical simulations (DNS) for low Reynolds number configurations ($Re = 2500$–5000) for comparison with other recent experimental results by Meunier (2001).

Only numerical predictions of the instability for the co-rotating case ($0 < \Lambda \leqslant 1$) are presented. Results related to the counter-rotating case $\Lambda = -1$ have been obtained by Laporte & Corjon (2000) at low Reynolds numbers for $a/b \simeq 0.25$. Although a/b

is close to the limit value imposed for the validity of the theory, good agreement with the present theoretical prediction has nevertheless been found for both the most unstable wavenumber of the first unstable branch, and its growth rate. These results have been extended to high Reynolds numbers and smaller a/b and excellent agreement has also been found (Laporte 2002).

7.1. *The numerical tool*

The numerical tool used to simulate the two-dimensional as well as the three-dimensional dynamics of the two-vortex flows is the NSMB 3D finite-volume Navier–Stokes solver developed in a European consortium including CERFACS. Both DNS and LES are performed with the NSMB code. This solver works on multi-blocks structured meshes. The simulations are performed using a four-stage Runge–Kutta method for the temporal integration. This method is fourth-order accurate when applied to a linear advection–diffusion equation. The advective terms are discretized with a fourth-order centred scheme developed at CERFACS (Ducros *et al.* 2000). This scheme is used without any addition of artificial dissipation. The diffusive terms are discretized with a standard second-order centred Jameson scheme. Large-eddy simulations are performed using the three times Filtered Structure Function subgrid-scale model (Ducros, Comte & Lesieur 1996) applied to the filtered Navier–Stokes equations. This model leads to the following expression for the turbulent viscosity at the point $\boldsymbol{x} = (x, y, z)$ and at the time t:

$$\nu_t(\boldsymbol{x}, \Delta_c, t) = 0.00084\,\Delta_c \sqrt{\tilde{F}_2^{(3)}(\boldsymbol{x}, \Delta_c, t)}, \tag{7.1}$$

where Δ_c is the cutoff length corresponding to the cutoff wavenumber $k_c = \pi/\Delta_c$. This length is defined by $\Delta_c = (\Delta_x \Delta_y \Delta_z)^{1/3}$, where Δ_i is the local cell size in the direction i. The superscript (3) indicates that the second-order velocity structure function $\tilde{F}_2$ is calculated using a velocity field filtered three times with a Laplacian filter. The second-order velocity structure function is defined as

$$\tilde{F}_2(\boldsymbol{x}, \Delta_c, t) = \langle \|\boldsymbol{u}(\boldsymbol{x} + \boldsymbol{r}, t) - \boldsymbol{u}(\boldsymbol{x}, t)\|^2 \rangle_{\|\boldsymbol{r}\| = \Delta_c}, \tag{7.2}$$

where $\langle\ \rangle$ denotes the average and $\boldsymbol{u}$, $\boldsymbol{x}$ and $\boldsymbol{r}$ are the resolved velocity vector, the position vector and the separation vector. This model does not add any turbulent viscosity for laminar flows as long as there is no energy at the cutoff wavelength. This feature is particularly important for the simulation of the transitional flows under consideration in the present paper.

7.2. *The numerical set-up*

The generic flow under consideration for the simulations is initially composed of a pair of co-rotating cylindric vortex tubes. Periodic boundary conditions are applied in the direction of the vortex axis.

In order to predict numerically the instability bands, the axial dimension L is systematically chosen to be equal to the wavelength of the potentially unstable mode whose growth rate is to be determined. This procedure enables the selection of the chosen mode to be enforced without simulating modes whose wavelength is close to the chosen wavelength. This procedure also allows the growth of modes with wavelengths equal to L/n to be captured where n is an integer depending on the axial discretization. In practice, $n \leqslant 3$ with the current discretization. In some other cases, the axial dimension L is set to $p\lambda$ where p is an integer and λ is the wavelength of the unstable mode to be computed (the corresponding wavenumber is $k = 2\pi/\lambda$).

This choice permits the simulation of the linear regime, but also the simulation of the nonlinear regime and the transition to a three-dimensional turbulent flow containing wavelengths larger than the elliptic wavelength. For all cases, the regular discretization in the axial direction is such that a wavelength of the elliptic mode to be simulated comprises 12 to 16 mesh points.

The mesh is locally refined in cross-flow planes in the region of the two vortices, so as to obtain 11 points in the vortex core radius. The boundaries in the corresponding directions are set far from the vortex system (the distance between one vortex and the closest cross-flow boundary is of the order of 6 times the initial vortex separation distance) and far-field boundary conditions are applied, by extrapolating the primitive variables using characteristic variables. This treatment aims at providing a non-reflecting boundary condition for the waves leaving the computational domain.

7.3. *The initial conditions*

Both the two-dimensional dynamics and the three-dimensional dynamics associated with the elliptical instability have been simulated. Two-dimensional simulations have been performed in order to assess the validity of the hypotheses made in §§ 2 and 4 for the modelling of the vortex system. They are also necessary to obtain the two-dimensional basic flow on which the evolution of three-dimensional perturbations is analysed. As already mentioned in § 4, the two-dimensional basic flow for given parameters a_1/b, a_2/b, Λ and Re_1 is obtained by a viscous relaxation process of an initial condition composed of two circular Gaussian vortices of the same circulation but smaller a_1/b and a_2/b. In all two-dimensional simulations, the same scenario, described in detail in Le Dizès & Verga (2002) for identical co-rotating vortices, has been observed. First, the initially circular vortices adapt to each other on a non-viscous time scale and their core becomes elliptical. The vortex system then reaches a quasi-steady state in the rotating frame. In fact, for the Reynolds numbers we have considered ($Re > 2500$), this state is, to a good approximation, a stationary solution of the Euler equations. Scatter plots, such as the one shown on figure 3 which demonstrates the functional relation between the vorticity ω and the streamfunction Ψ (for the configuration without straining), can be used to check this property.

However, the vortex system slowly evolves due to viscous diffusion. As demonstrated in Le Dizès & Verga (2002), the main effect of viscosity is to increase of the vortex size, which evolves according to (2.8). It is this latter property which is used to obtain a two-dimensional flow of given parameters a_1/b and a_2/b. Let us denote by (u, v) such a two-dimensional two-vortex flow. A three-dimensional white noise is added to the unperturbed local velocity vector $(u, v, w)^T$ to obtain the initial perturbed velocity field $(u_0, v_0, w_0)^T$ that will trigger the elliptic instability. The local perturbation procedure applied at each grid point of the three-dimensional space is

$$\left.\begin{aligned} u_0 &= u \times (1 + rA), \\ v_0 &= v \times (1 + rA), \\ w_0 &= 0, \end{aligned}\right\} \tag{7.3}$$

where $r = r(x, y, z)$ is a local random number in the range $[-1/2, 1/2]$, and A a fixed perturbation amplitude. In the simulations, A is chosen between 10^{-6} and 10^{-3}.

The evolution of the amplitude of the instability mode is obtained by the following procedure. A signal associated with a single vortex is first obtained by averaging the instantaneous local kinetic energy over the domain D_1. This provides the kinetic energy as a function of the axial direction z. The square root of this signal is then

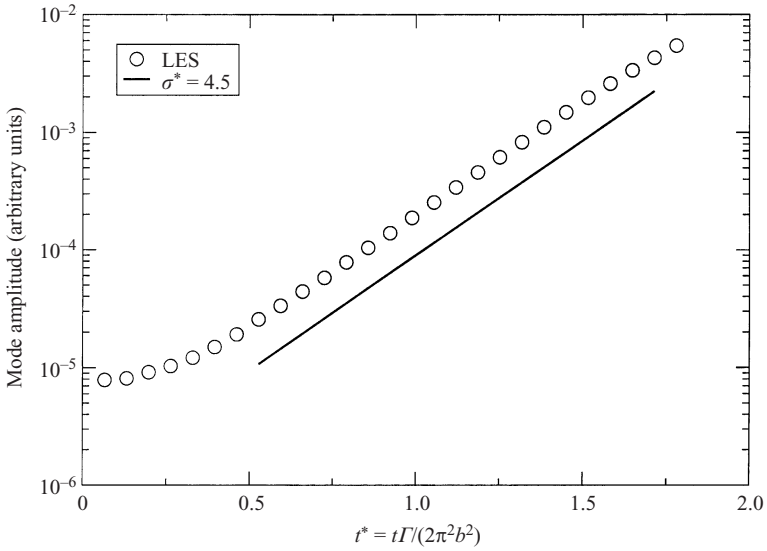

FIGURE 9. Typical evolution of the unstable mode amplitude as a function of the non-dimensional time $t^* = t\Gamma/(2\pi^2 b^2)$, for the system $\Lambda = 1$, $a_1/b = a_2/b = a/b = 0.15$, $Re = 5 \times 10^5$, $\lambda/a = 3.25$.

decomposed into Fourier modes. The growth rate of the instability is finally obtained from the time evolution of the most amplified Fourier mode. More details on this procedure are given in Laporte & Corjon (2000).

7.4. *Results for the symmetric case* $\Lambda = 1$

For the symmetric case $\Lambda = 1$, $a_1 = a_2 = a$, three different sets of parameter have been considered. A reference case for small a/b and large Reynolds number was first performed for a single axial wavelength to test the validity of the theory with a parameter clearly within the bounds imposed by the theory. A complete instability diagram is also obtained by varying the axial wavelength for a larger parameter a/b. This set of simulations enables comparison of the first two instability bands as obtained by the simulation and by the theory. Finally, some simulations have been performed at low Reynolds numbers in order to provide comparisons with the viscous prediction and experimental results.

The reference case is defined by the configuration $a/b = 0.15$ and the Reynolds number $Re = 5 \times 10^5$. For this case, the LES version of the code is used, simulating a domain of axial dimension corresponding to the non-dimensional wavelength $\lambda/a = 3.25$. Figure 9 presents the evolution of the amplitude of the unstable elliptic mode as obtained by the Fourier analysis described above. The wavelength corresponds to the theoretically most unstable wavelength of the first branch for this case, $\lambda/a = 3.25$. The linear regime (corresponding to an exponential growth of the elliptic mode) is simulated, and the evolution towards the saturation of the unstable mode can be observed through the stabilization of the mode in the nonlinear regime. The non-dimensional growth rate obtained in the linear regime is

$$\sigma^* = \sigma \frac{2\pi^2 b^2}{\Gamma} \simeq 4.5, \tag{7.4}$$

which is reasonably close to the value $\sigma^* = 4.86$ (7% relative error) obtained from

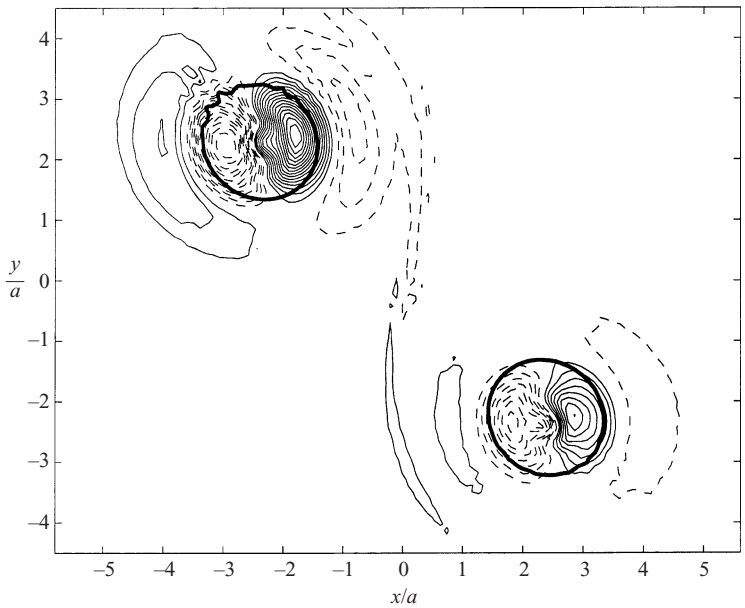

FIGURE 10. Typical contour plot for the perturbation axial velocity in a plane perpendicular to the vortex axes for two identical co-rotating vortices. System parameters are the same as in figure 9 and $t^* = 1.31$. Solid lines (resp. dashed lines) correspond to positive velocities (resp. negative velocities). Vortex cores are represented by thick solid lines ($\omega/\omega_{\max} = 1/e$).

formula (6.1). Note that for this Reynolds number, the viscous correction is almost equal to the inviscid prediction, which is $\sigma^* = 4.89$.

On figure 10 are displayed the axial velocity contours for the perturbation in a plane perpendicular to the vortex axis at the end of the linear regime. The two-lobes structure, characteristic of the helical modes $m_1 = 1$ and $m_2 = -1$, is clearly visible and very similar to theoretical predictions for the elliptic instability (Waleffe 1990). Moreover, the perturbation structure is oriented perpendicularly to the direction of stretching in each vortex (which is approximatively vertical in figure 10) in agreement with the linear instability mechanism. This observation constitutes a validation of the resonance mechanism between the Kelvin modes $m_1 = 1$ and $m_2 = -1$ described in § 5. It also justifies the hypothesis made in § 2 for not having considered other sources of instability in the flow. In particular, no influence of the local instability near the hyperbolic points of the system has been detected.

Note that the perturbation axial velocity in both vortices is here antisymmetrical with respect to the central hyperbolic point. This means that the perturbation axial vorticity is also antisymmetrical with respect to that point. Core deformations are thus in phase in each vortex as illustrated below in figure 13(a).

Because the instability is initially triggered by injecting a white noise into the flow, the subgrid-scale model may detect the presence of energy at the cutoff wavelength for large Reynolds numbers. As a consequence, the numerical model may react by dissipating this energy as if it were isotropic and homogeneous turbulence. This artificial addition of turbulent viscosity ν_t (recall that the total viscosity ν_{tot} in the flow is $\nu_{tot} = \nu + \nu_t$, where ν is the kinematic viscosity) is in fact responsible for a global decrease of the Reynolds number in the flow. This effect depends on the initial amplitude of the white noise, and may be minimized by damping the initial

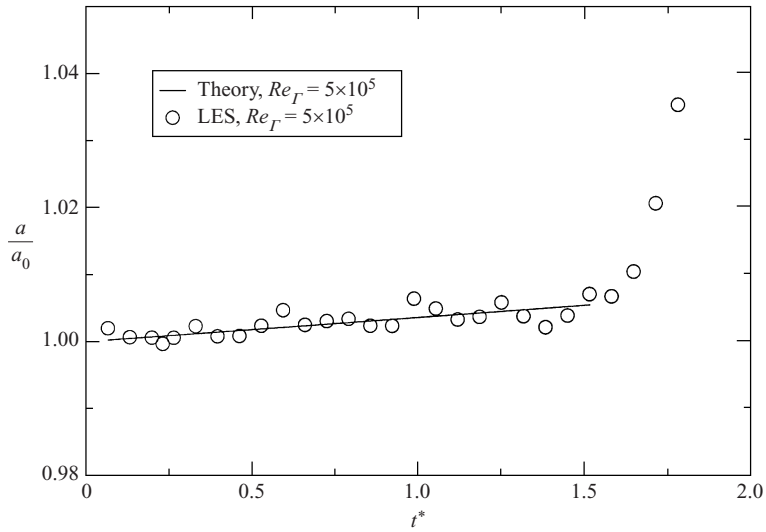

FIGURE 11. Evolution of the normalized vortex core radius a/a_0 in the simulation. The theoretical core evolution (7.5) corresponding to $Re = 5 \times 10^5$ is also presented.

energy at the cutoff wavelength (such a procedure has been applied for this particular simulation). An estimation of the effective Reynolds number in the flow may be obtained by measuring the evolution of the vortex core sizes, which evolve as

$$a(t) = \sqrt{4\nu_{tot}t + a_0^2}, \tag{7.5}$$

and permits the determination of ν_{tot}, and consequently of the effective Reynolds number $Re^{eff} = \Gamma/\nu_{tot}$. For the present case, the procedure minimizing the artificial dissipation effect has been proved to be efficient. In figure 11 the effective core evolution measured in the flow is compared to the theoretical evolution given by equation (7.5) for $Re = 5 \times 10^5$. The two results are essentially the same in the linear regime (the differences are smaller than the measurement errors), therefore we have $\nu_{tot} = \nu$ and $Re^{eff} = Re$. This constitutes an *a posteriori* validation of the expected neutral behaviour of the subgrid-scale model in the linear regime. In the nonlinear regime, as soon as the transition to turbulence starts, the vortex radius increases as expected.

The complete set of large-eddy simulations has been performed at the Reynolds number $Re = 10^5$ for the case $a/b = 0.21$, by varying the axial dimension of the calculation domain in the range $1.35 \leqslant L/a \leqslant 5.95$. The numerical results are compared with the theory in figure 12, where the non-dimensional growth rates are plotted against the non-dimensional wavelength of the mode. The numerical growth rates are obtained by a Fourier analysis in the axial direction, as for the previous case. The numerical results in the linear regime are shown by the circles, whereas the solid lines are formula (6.1) for the first three unstable bands ($n = 0, 1, 2$). The overall agreement between the simulated growth rates and the predicted unstable bands is good, despite the fact that the parameter a/b is large, and close to the limit imposed by the theory. This means that reliable predictions may be obtained with the present theory for configurations close to the merging limit ($a/b \simeq 0.23$) in the symmetric case $\Lambda = 1$, $a_1 = a_2 = a$.

Note also the good agreement of the numerical results with formula (6.1) outside

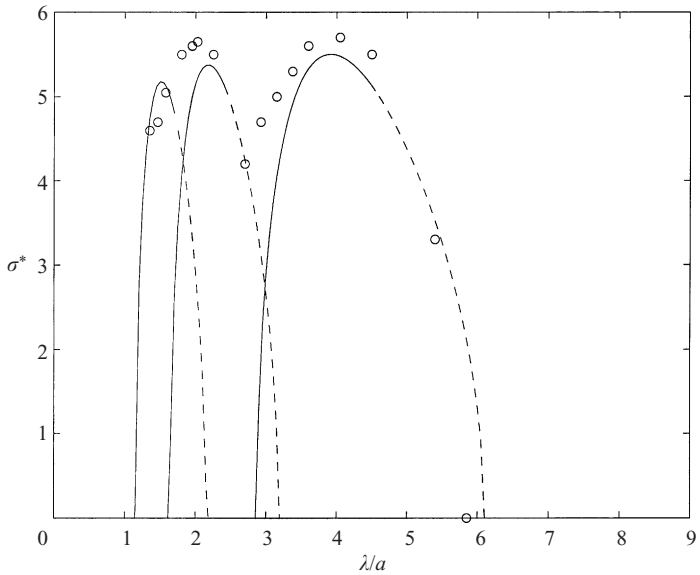

FIGURE 12. Unstable bands as predicted by numerical simulations (circles) and by the theory for the first three unstable bands (solid lines becoming dashed lines outside the theoretical limits) for the vortex system $A = 1$, $a_1/b = a_2/b = a/b = 0.21$, $Re = 10^5$.

the theoretical limits imposed in § 5 (dashed lines in figure 12). As explained in § 5, outside these limits, no resonance of linear Kelvin modes leading to instability should be possible as the linear modes are strongly damped. Instability therefore means that the Kelvin modes are not as damped as expected. This could be the signature of the appearance of nonlinearity in the characteristics of the Kelvin modes.

So far, very large Reynolds numbers have been considered for which viscous effects on the perturbation were negligible. It is therefore interesting to consider configurations for which this is no longer the case. Results obtained by direct numerical simulations for $Re = 2500$ and $Re = 5000$ are now presented. These simulations were also motivated by recent results by Meunier & Leweke (2001) who experimentally investigated the instability for such low Reynolds numbers. Their experimental results have been proved to be satisfactory (Leweke *et al.* 2001), despite the difficulty in analysing the instability characteristics in these regimes. One of the difficulties is due to the influence of viscous diffusion on the instability characteristics. Indeed, one of the basic assumption of the linear stability analysis is that the instability time scale $T_a = 2\pi^2 b^2/\Gamma$ should remain much smaller than the viscous evolution time scale $T_v = 2\pi a^2/\nu$ of the basic flow. The ratio of these two time scales is

$$\frac{T_a}{T_v} = \frac{\pi}{Re(a/b)^2}. \tag{7.6}$$

For a two-vortex flow at $Re = 2500$, the above ratio becomes small (say smaller than 0.1) when $a/b > 0.12$ only. This means than the time-scale separation needed to justify the linear stability analysis is not satisfied for $a/b < 0.12$. As a/b increases with time, the time scales separate progressively and the stability analysis becomes increasingly valid, provided that other rapid phenomena such as vortex merging have not started. The vortex merging phenomenon provides the second limitation. For a two-dimensional flow, it starts for $a/b \approx 0.23$ (Meunier *et al.* 2002). However, it is not

Re	a/b	λ/a	σ^{num}	σ_V^{th}	σ_{NV}^{th}	σ^{exp}
2700	0.212	3.6	3.8	3.12	5.41	3.5 ± 0.5
5000	0.203	3.8	5.0	4.2	5.45	

TABLE 1. Comparison of simulated and predicted unstable elliptic mode characteristics for different Reynolds number and parameter a/b. The growth rates provided by the numerical simulation, the viscous theoretical prediction and the inviscid prediction are denoted respectively by σ^{num}, σ_V^{th} and σ_{NV}^{th}. The last column σ^{exp} corresponds to experimental results by Meunier & Leweke (private communication, see also Meunier 2001).

impossible that it occurs earlier in presence of a three-dimensional instability. Thus it may have an influence on the instability characteristics for smaller a/b.

The initial configurations in the simulations have been chosen to be very close to the initial measurements of Meunier & Leweke, which approximately correspond to $a_0/b \simeq 0.15$. In the simulations, as in the experiments, a delay is always observed before the unstable mode starts being amplified. During this period, the flow configuration evolves through viscous effects, so that a/b increases. Therefore the instability analysis must be based on the instantaneous a/b corresponding to the onset of the linear regime of the instability. This procedure has been applied here. Note also that the finite axial dimension of the simulation domain allows only a finite number of unstable modes within each unstable band to be predicted. Due to the viscous effects on the parameter a/b, it is therefore very unlikely that the mode associated with the most unstable wavelength will be simulated exactly. Table 1 presents the results obtained for different Reynolds numbers and different flow configurations.

The simulated growth rates are found to be systematically larger than the viscous predictions, but always lie between the viscous and the inviscid predictions. The relative error between simulation and theory is of the order of 20% for the lower Reynolds numbers, while it was within 10% for the large Reynolds number configurations studied above. This is slightly surprising as one would have expected time-dependent effects associated with low Reynolds numbers to remain smaller. A similar underestimation of the growth rate was also noted in Meunier (2001) where experimental results are also compared with the present theory for different Reynolds numbers. We have no clear explanation for such a discrepancy. As mentioned above, it could be due to an insufficient time-scale separation or to an interaction with the merging process. Another cause could be the effect of viscosity on the Kelvin mode characteristics. In the theory, we have used the Kelvin mode characteristics for infinite Reynolds numbers. For low Reynolds numbers, this could become a crude approximation. Fabre (2002) recently analysed the evolution of the Kelvin mode characteristics for Reynolds numbers ranging from $Re = 10^3$ to 10^5. He showed that for $Re \geqslant 10^4$ the infinite Reynolds number estimate for the frequency is very good whatever the wavenumber. For $Re = 10^3$, a weak discrepancy becomes visible, notably near the wavenumbers in figure 6 for which the frequency departs from the linear fit. Fabre showed that viscous effects tend to decrease the frequency of the Kelvin mode $m = 1$. Here, this would affect the Kelvin modes resonance by slightly shifting the instability bands towards larger wavelengths. Viscous damping would therefore be smaller. Thus, taking into account viscous effects in the Kelvin mode characteristics could increase the theoretical growth rate and diminish the differences observed between theory and experiments.

Figure 13 presents the complete two-vortex flow dynamics from the linear regime

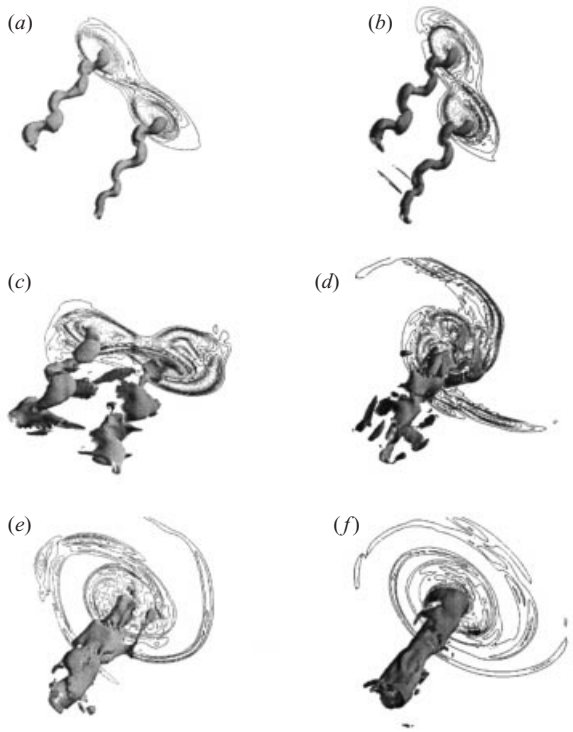

FIGURE 13. Linear and nonlinear regimes of the instability leading to the unstable merging at $Re = 5 \times 10^4$ for a symmetric configuration $\Lambda = 1$ defined by $a_1/b = a_2/b = 0.178$. Isocontours and isosurfaces of the vorticity magnitude are plotted at times (*a*) $t^* = 1.1$, (*b*) $t^* = 1.2$, (*c*) $t^* = 1.4$, (*d*) $t^* = 1.7$, (*e*) $t^* = 1.9$ and (*f*) $t^* = 2.2$.

for $Re = 5 \times 10^4$. The nonlinear regime, the saturation, and the local transition to a turbulent flow which ultimately relaminarizes to form a single and well-defined vortex can be observed. The visualization at the end of the linear regime (time $t^* = 1.1$) provides information on the instability mode, which is seen to induce an in-phase undulation of each vortex core. Such an undulation has also been observed in experiments (Meunier 2001). The in-phase character of the undulations cannot be explained by our approach as we do not consider any coupling between the perturbation modes of each vortex. Sipp (1999) analysed this coupling for two counter-rotating vortices by considering the linear stability of the pair. He showed that for $a/b < 0.2$, symmetric and antisymmetric modes have the same growth rate and that above $a/b > 0.2$, the antisymmetric mode leading to in-phase undulations is only slightly more amplified. He argued that the experimental results (Leweke & Williamson 1998) where in-phase undulations are almost systematically observed cannot be explained by a linear selection of the instability mode. Direct simulations by Laporte (2002) also systematically show in-phase undulations for $a/b > 0.15$. Laporte (2002) however succeeded in exhibiting uncoupled modes for very small $a/b \approx 0.1$. Although these results are for counter-rotating vortices, one could expect similar results to apply to co-rotating vortices. In particular, one could easily imagine that uncoupled instability modes exists for very small a/b, and that above a critical value of a/b, which is probably close to 0.15, the antisymmetric mode giving rise

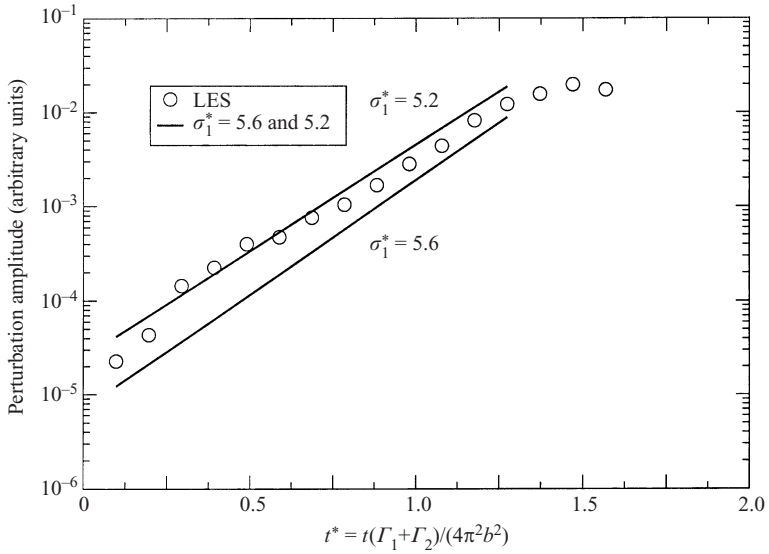

FIGURE 14. Evolution of the kinetic energy of the unstable mode of vortex Γ_1 for the configuration $\Lambda = \Gamma_1/\Gamma_2 = 0.7$, $a_1/b = 0.15$, $a_2/b = 0.18$ and $Re_2 = 10^6$. The wavelength of the amplified mode is $\lambda/a_1 = 3.35$.

to in-phase undulations is selected by the nonlinear dynamics. Here we have not considered sufficiently small values of a/b to observe uncoupled undulations.

From figure 13, note also that the merging process which occurs between $t^* = 1.4$ and $t^* = 1.9$ implies very complex three-dimensional dynamics. This affects the characteristics of the final vortex which are significantly different from the characteristics that would have been obtained after a two-dimensional merging (see also Meunier & Leweke 2001, concerning this point). As mentioned above, the critical a/b threshold for two-dimensional merging is approximately $a/b = 0.23$ for symmetric vortex dipoles. This criterion is purely two-dimensional, and would certainly not apply in the present three-dimensional flow configuration. In fact, merging can occur either from the two-dimensional dynamics that were recalled earlier, or from the elliptic instability as simulated here. In the present case, the initial parameter a/b leading to merging via the elliptic instability is smaller than the threshold given by the two-dimensional criterion. Similar observations were made by Meunier & Leweke (2001).

7.5. *A result for the asymmetric case* $\Lambda < 1$

A single three-dimensional large-eddy simulation has been performed for the asymmetric case $\Lambda = \Gamma_1/\Gamma_2 = 0.7$. The configuration is defined by $a_1/b = 0.15$ and $a_2/b = 0.18$ at the Reynolds number $Re_2 = 10^6$. The axial length of the computational domain is $L/a_1 = 3.35$, corresponding to the theoretically most unstable wavelength of the first instability band, for vortex Γ_1. The theory also predicts that the instability is stronger in vortex Γ_1 than in vortex Γ_2. For vortex Γ_1, the non-dimensional growth rate obtained by the Fourier analysis is between $\sigma_1^* = 5.2$ and $\sigma_1^* = 5.6$ for the non-dimensional wavelength $\lambda/a_1 = 3.35$ (figure 14). The theoretical prediction obtained from formula (6.1*a*) for this wavelength is $\sigma_1^* = 5.87$ which differs between 5% and 12% from the numerical value. Thus, there is a good agreement between simulation and theory.

The axial box length L allows the simulation of all the modes of wavelengths

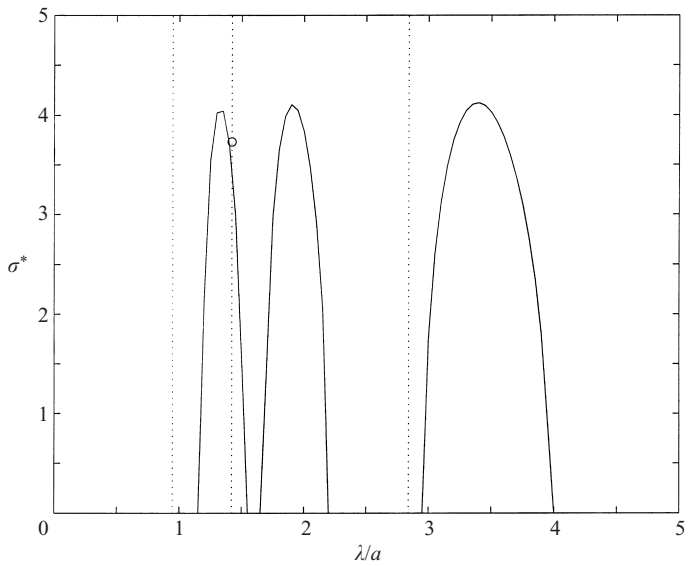

FIGURE 15. Comparison between simulation and theory for vortex Γ_2 in the asymmetric configuration ($\Lambda = 0.7$, $a_1/b = 0.15$, $a_2/b = 0.18$, $Re_2 = 10^6$). The simulated growth rate is shown by a circle, whereas the first three instability bands predicted by the theory are displayed as solid lines. The vertical dotted lines indicate the instability wavelengths which were possible in the simulation.

$\lambda_p = L/p, p = 1, 2, 3, \ldots$ in both vortices. Figure 15 displays for vortex Γ_2 the first three unstable bands (solid lines) given by formula (6.1b) for $n = 0, 1, 2$, and the first axial normalized wavelengths $\lambda_p/a_2 = L/(pa_2)$ (dotted lines) that can be simulated with the given axial length L. As can be observed, the largest unstable wavelength that can be simulated corresponds to the second axial Fourier mode $p = 2$, and belongs to the third instability band. This mode of wavelength $\lambda/a_2 = 1.42$ is indeed the mode observed in the simulation. Its growth rate $\sigma_2^* = 3.73$, shown by a circle on figure 15 is very close to the theoretical prediction.

In conclusion, the successful comparison made here for both vortices Γ_1 and Γ_2 is a further validation of the linear theory for asymmetric cases.

8. Discussion

In this paper, we have considered the linear stability of a generic flow composed of two parallel Gaussian vortices of different circulations and vortex radii when the flow is quasi-steady in the frame of reference rotating with the vortex system. Validity limits associated with the quasi-steadiness constraint have been provided in terms of global characteristics of the two-dimensional vortex system by analytical considerations and numerical simulations. Both vortices have been shown to be potentially unstable (with different instability characteristics) to three-dimensional perturbations, due to the elliptic deformation of their core. Such a deformation is due to the strain induced by one vortex on the other. The analysis has provided the viscous growth rate of the global instability modes from local stability considerations in the centre of each vortex. An explicit formula for the elliptic instability has been used, which depends on two undetermined coefficients. These coefficients are the (internal) strain rate in the centre of the vortex, and the orientation angle of the local perturbation wavevector. The internal strain rate is obtained by assuming that each is vortex alone in a

uniform rotating external strain field whose characteristics are provided by a point vortex model. This has permitted application of an existing relation linking internal and external strain rates. Direct numerical simulations of several two-vortex flows have been performed to validate the expression obtained for the strain rate. The orientation angle of the local perturbation wavevector has been determined by using the linear normal-mode description of the elliptical instability. It has been argued that the most unstable elliptical modes are necessarily a combination of two Kelvin modes of azimuthal wavenumbers $m = 1$ and $m = -1$, which has allowed the determination of the orientation angle from the dispersion relation of the Kelvin mode $m = 1$. The final formula, which gives the growth rate as a function of the axial wavenumber, has been tested using direct numerical simulations and large-eddy simulations. A good agreement for high Reynolds number flows ($Re > 10^5$) has been demonstrated for both symmetric and asymmetric configurations. An underestimation of 20% by the theory has also been noted for small Reynolds numbers ($Re = 2500$–5000). Specific difficulties associated with small Reynolds number flows have been discussed and possible causes of the weak discrepancy have been provided.

In summary, the theoretical formula has been shown to provide a good or fairly good estimate for the instability growth rate in all the configurations we have simulated. A similar good agreement with experimental results has also been obtained elsewhere (Meunier 2001).

The generic two-vortex flow analysed in the present paper may be found in a large number of different flows. In the aeronautical context, the wake shed by an aircraft may initially be composed of several co- and counter-rotating vortices, depending on the spanwise load distribution on the wings and the high-lift elements. For example a wing equipped with a single flap generates in the near field a wing-tip vortex and a co-rotating outboard flap-tip vortex. In general, these vortices may have different vortex core sizes and circulations. They are also well separated in the near field, so that the stability analysis of this asymmetric two-vortex flow may be obtained by the present analysis, provided that the flow may be assumed to be locally parallel and the axial velocity negligible. Spatial and temporal simulations by the second author have shown that such realistic asymmetric flap-tip vortex systems are indeed unstable (Laporte 2002). The elliptic instability has been demonstrated to develop in both vortices and the instability has been proved to be convective. In general, the co-rotating vortices generated by the flap and the wing tips merge at a finite distance from their generation point. Then a single vortex remains downstream of each wing. The complete wake is then composed of a single counter-rotating symmetric vortex pair. Again, the present theory applies to this two-vortex flow. Note that asymmetric counter-rotating vortices may also be found for wings equipped with multiple flaps. All the cited cases show that the growth formula provided by the linear theory may be of interest to detect the most unstable flow configurations that could be exploited to destabilize the vortex system and that could ultimately result in a faster decay of the wake vortices. Once the selection of the most unstable flow configurations is made, the numerical simulation or experiments may be used as a necessary complement to assess the transition regime and the late stages that result from the instability mechanism, and that are relevant in the case of an aircraft/vortex encounter.

This work has benefitted from discussions with Patrice Meunier and Thomas Leweke. We would like to thank them for having communicated their experimental results all along this work. Financial support by DGA, contract number 97-1097 (SLD) is also gratefully acknowledged.

REFERENCES

Balmforth, N. J., Llewellyn Smith, S. G. & Young, W. R. 2001 Disturbing vortices. *J. Fluid Mech.* **426**, 95–133.

Bassom, A. P. & Gilbert, A. D. 1998 The spiral wind-up of vorticity in an inviscid planar vortex. *J. Fluid Mech.* **371**, 109–140.

Batchelor, G. K. 1967 *An Introduction to Fluid Dynamics*. Cambridge University Press.

Bayly, B. J. 1986 Three-dimensional instability of elliptical flow. *Phys. Rev. Lett.* **57**, 2160–2163.

Bernoff, A. J. & Lingevitch, J. F. 1994 Rapid relaxation of an axisymmetric vortex. *Phys. Fluids* **6**, 3717–3723.

Billant, P., Brancher, P. & Chomaz, J.-M. 1999 Three-dimensional stability of a vortex pair. *Phys. Fluids* **11**, 2069–2077.

Briggs, R. J., Daugherty, J. D. & Levy, R. H. 1970 Role of Landau damping in cross-field electron beams and inviscid shear flow. *Phys. Fluids* **13**, 421–432.

Couder, Y. 1983 Observation expérimentale de la turbulence bidimensionnelle dans un film liquide mince. *C. R. Acad. Sc. Paris* II **297**, 641–645.

Dritschel, D. G. & Waugh, D. W. 1992 Quantification of the inelastic interaction of unequal vortices in two-dimensional vortex dynamics. *Phys. Fluids* A **4**, 1737–1744.

Ducros, F., Comte, P. & Lesieur, M. 1996 Large-eddy simulation of transition to turbulence in a boundary layer spatially developing over a flat plate. *J. Fluid Mech.* **326**, 1–36.

Ducros, F., Laporte, F., Souleres, T., Guinot, V., Moinat, P. & Caruelle, B. 2000 High-order fluxes for conservative skew-symmetric-like schemes in structured meshes: application to compressible flows. *J. Comput. Phys.* **161**, 114–139.

Eloy, C. & Le Dizès, S. 1999 Three-dimensional instability of Burgers and Lamb–Oseen vortices in a strain field. *J. Fluid Mech.* **378**, 145–166.

Eloy, C. & Le Dizès, S. 2001 Stability of the Rankine vortex in a multipolar strain field. *Phys. Fluids* **13**, 660–676.

Fabre, D. 2002 Instabilitités et instationnarités dans les tourbillons: application aux sillages d'avions. PhD thesis, ONERA/Université Paris VI.

Hopfinger, E. J. & van Heijst, G. J. F. 1993 Vortices in rotating fluids. *Annu. Rev. Fluid Mech.* **25**, 241–289.

Huerre, P. & Monkewitz, P. A. 1990 Local and global instabilities in spatially developing flows. *Annu. Rev. Fluid Mech.* **22**, 473–537.

Jiménez, J., Moffatt, H. K. & Vasco, C. 1996 The structure of the vortices in freely decaying two dimensional turbulence. *J. Fluid Mech.* **313**, 209–222.

Kerswell, R. R. 2002 Elliptical instability. *Annu. Rev. Fluid Mech.* **34**, 83–113.

Landman, M. J. & Saffman, P. G. 1987 The three-dimensional instability of strained vortices in a viscous fluid. *Phys. Fluids* **30**, 2339–2342.

Laporte, F. 2002 Simulation numérique appliquée à la caractérisation et aux instabilités des tourbillons de sillage des avions de transport. PhD thesis, Institut National Polytechnique de Toulouse, CERFACS.

Laporte, F. & Corjon, A. 2000 Direct numerical simulations of the elliptic instability of a vortex pair. *Phys. Fluids* **12**, 1016–1031.

Leblanc, S. 1997 Stability of stagnation points in rotating flows. *Phys. Fluids* **9**, 3566–3569.

Le Dizès, S. 2000*a* Non-axisymmetric vortices in two-dimensional flows. *J. Fluid Mech.* **406**, 175–198.

Le Dizès, S. 2000*b* Three-dimensional instability of a multipolar vortex in a rotating flow. *Phys. Fluids* **12**, 2762–2774.

Le Dizès, S. & Verga, A. 2002 Viscous interactions of two co-rotating vortices before merging. *J. Fluid Mech.* **467**, 389–410.

Leweke T., Meunier, P., Laporte, F. & Darracq, D. 2001 Controlled interaction of co-rotating vortices. *3rd ONERA-DLR Aerospace Symposium, ODAS, Paris*, (ed. K. Bütefisch *et al.*).

Leweke, T. & Williamson, C. H. K. 1998 Cooperative elliptic instability of a vortex pair. *J. Fluid Mech.* **360**, 85–119.

Lifschitz, A. & Hameiri, E. 1991 Local stability conditions in fluid dynamics. *Phys. Fluids* A **3**, 2644–2651.

Lin, C. C. 1955 *The Theory of Hydrodynamics Stability*. Cambridge University Press.

Melander, M. V., McWilliams, J. C. & Zabusky, N. J. 1987 Axisymmetrization and vorticity-

gradient intensification of an isolated two-dimensional vortex through filamentation. *J. Fluid Mech.* **178**, 137–159.

Meunier, P. 2001 étude expérimentale de deux tourbillons corotatifs. PhD thesis, Université d'Aix-Marseille 1.

Meunier, P., Ehrenstein, U., Leweke, T. & Rossi, M. 2002 A merging criterion for two-dimensional co-rotating vortices. *Phys. Fluids* **14**, 2757–2766.

Meunier, P. & Leweke, T. 2001 Three-dimensional instability during vortex merging. *Phys. Fluids* **13**, 2747–2750.

Mitchell, T. B. & Driscoll, C. F. 1996 Electron vortex orbits and merger. *Phys. Fluids* **8**, 1828–1841.

Moffatt, H. K., Kida, S. & Ohkitani, K. 1994 Stretched vortices – the sinews of turbulence; large-Reynolds-number asymptotics. *J. Fluid Mech.* **259**, 241–264.

Moore, D. W. & Saffman, P. G. 1971 Structure of a line vortex in an imposed strain. In *Aircraft Wake Turbulence* (ed. R. Olsen, P. Golburg & M. Rogers), pp. 339–354. Plenum.

Moore, D. W. & Saffman, P. G. 1975 The instability of a straight vortex filament in a strain field. *Proc. R. Soc. Lond.* A **346**, 413–425.

Overman, E. A. & Zabusky, N. J. 1982 Evolution and merger of isolated vortex structures. *Phys. Fluids* **25**, 1297–1305.

Prochazka, A. & Pullin, D. I. 1995 On the two-dimensional stability of the axisymmetric Burgers vortex. *Phys. Fluids* **7**, 1788–1790.

Saffman, P. G. 1992 *Vortex Dynamics*. Cambridge University Press.

Schecter, D. A., Dubin, D. H. E., Cass, A. C., Driscoll, C. F., Lansky, I. M. & O'Neil, T. M. 2000 Inviscid damping of asymmetries on a two-dimensional vortex. *Phys. Fluids* **12**, 2397–2412.

Sipp, D. 1999 Instabilités dans les écoulements tourbillonnaires. PhD thesis, Ecole polytechnique, Palaiseau.

Sipp, D., Jacquin, L. & Cossu, C. 2000 Self-adaptation and viscous selection in concentrated two-dimensional dipoles. *Phys. Fluids* **12**, 245–248.

Ting, L. & Tung, C. 1965 Motion and decay of a vortex in a nonuniform stream. *Phys. Fluids* **8**, 1039–1051.

Trieling, R. R., Beckers, M. & van Heijst, G. J. F. 1997 Dynamics of monopolar vortices in a strain flow. *J. Fluid Mech.* **345**, 165–201.

Trieling, R. R., Linsen, A. H. & van Heijst, G. J. F. 1998 Monopolar vortices in an irrotational annular shear flow. *J. Fluid Mech.* **360**, 273–294.

Waleffe, F. 1990 On the three-dimensional instability of strained vortices. *Phys. Fluids* A **2**, 76–80.

Weiss, J. B. & McWilliams, J. C. 1993 Temporal scaling behavior of decaying two-dimensional turbulence. *Phys. Fluids* A **5**, 608–621.